Direct Laser Scribed MoO_2-based Materials and Their Applications in Bioelectronics and Soft Robotics

---

A Thesis

presented to

the Faculty of the Graduate School

at the University of Missouri-Columbia

In Partial Fulfillment

of the Requirements for the Degree

Master of Science

---

by

Zanyu Chen

Dr. Zheng Yan, Thesis Supervisor

DEC 2021

The undersigned, appointed by the Dean of the Graduate School, have examined the

thesis entitled

presented by Zanyu Chen,

a candidate for the degree of Master of Science,

and hereby certify that, in their opinion, it is worthy of acceptance.

_____

Professor Zheng Yan

_____

Professor Qingsong Yu

_____

Professor Mahmoud Almasri

ACKNOWLEDGEMENTS

CONTENTS

ABSTRACT

Overcoming the disadvantages of rigid traditional electronic materials, flexible epidermal electronics with soft, elastic and mechanically conformable characteristics are capturing wide attention. In order to meet the requirements of high conductivity of current path and base electrode and good biocompatibility, high sensitivity and stability of monitoring sensor for skin wearable devices, we developed direct laser scribing MoO_2 (DLS-MoO_2) high conductive trace on breathable, flexible and chemical stability porous SEBS substrate. And by following electrode modifications and functionalization, we fabricated multifunctional flexible sensors including electrophysiological sensors, temperature sensor, UV sensor, humidity sensor, alcohol sensor, and NH_3 sensor. Furthermore, photo-actuating soft robotics based on the photothermal transformation of MoO_2 have also been developed.

Chapter 1. Introduction

1.1 Application and development potential of flexible electronics and devices

Skin-Interfaced Electronics that combine the inherent characteristics of polymers and flexible electronics and overcomes the shortcomings of noise and artifacts caused by air gaps when rigid traditional electronic materials come into contact with objects, are capturing wide attention[1-6]. The resulting electronic materials and devices are soft, elastic and mechanically conformable[4], and can improve user comfort and minimize adverse reactions[7-10]. These characteristics of interaction with biological systems are important qualities for flexible bioelectronic applications in wearable devices[4].

In various types of flexible electronic devices, sensors play a crucial role. Wearable biosensors can provide continuous and real-time physiological information by dynamically and measurably measuring biochemical markers in biological fluids. In earlier studies, attention was mainly focused on physical sensors that monitor mobility and vital signs, and the main indicators monitored were step counts, burned calories, or heart rate. Recently, the focus of research has shifted to biosensors, and the main monitoring indicators have changed into human physiological signals, such as body temperature, skin impedance, and human electrophysiological information, such as electrocardiogram (ECG), electroencephalogram (EEG), and electromyography (EMG).

Research and Application of Flexible Electronics and Devices in Wearable

Biosensors

Flexible electrodes coupled with screen printing can directly and continuously contact the skin surface and measure key-sweat electrolytes consisting of inorganic ions, nutrients, and metabolites in real time[11-17]. J.W. et.al. found that continuous monitoring of sweat lactate levels by epidermal electrochemical biosensors reflects the real-time characteristics of lactate sweat dynamics during exercise, thereby monitoring physical exertion levels during prolonged exercise, which in turn assesses exercise efficiency[15]. The Berkeley team achieved the integration of multi-sensor arrays by fusing flexible patch-type sensors with contoured circuit boards to simultaneously detect sweat metabolites (glucose and lactate) and electrolytes (sodium and potassium ions), as well as skin temperature, and this pioneering work strongly advanced the field of wearable sensing by filling the gap between signal transduction, conditioning, data processing, wireless transmission, and system integration allowing in suit data processing and communication[18]. Recent studies have shown that multi-analyte electrochemical sensing fibers, which weave multiple sensing fibers into a soft fabric, maintain attractive real-time sensing performance under repeated deformation, and their reliable in situ multi-analyte monitoring can effectively improve the ability of personalized diagnosis and monitoring of individual wearable devices[19]. J.W. et.al. found that through screen printing of electrodes for reverse iontophoresis and glucose biosensing electrodes, the price of the sensing platform for reverse iontophoresis is not only greatly reduced, the discomfort during reverse iontophoresis is minimized, but also it is easy to install on the skin surface without hindering the movement of the wearer[18].

There have also been several recent studies on extended target biomarkers, including those related to hormones and immune responses, such as biosensors that detect cortisol and interleukin-6 in sweat[20]. In addition, researchers have reported a MoS_2 nanosheet based on cortisol antibody functionalization that can replace the original cortisol detection system[21]. Although such antibody-based bioassays have created more possibilities for the development of epidermal wearable biosensors, whether they can be successfully used in humans has yet to be demonstrated.

Research and application of flexible electronic materials in ocular wearable biosensors.

A recent advance in wearable contact lens biosensors is optical continuous glucose monitoring through the employing of smartphones[22]. Hydrogel sensors with photonic microstructures were attached to a commercial contact lens mountain and reflectance was recorded using a smartphone to reflect changes in tear glucose. The electronic device has the advantages of simple manufacturing, rapid and sensitive response to glucose changes. In addition, NovioSense has designed a small spring-like electrochemical sensor consisting of multiple coiled wire electrodes coated with a polysaccharide-based protective hydrogel material. This sensor is placed at the bottom of the glasses, and when combined with wireless data transmission, it can provide continuous tear glucose measurements without causing ocular discomfort.

Research and application of flexible electronic materials in oral wearable biosensors

Mannoor et. al. reported printing graphene-based nanosensors on water-soluble

silk and directly transferred to enamel for the detection of salivary bacteria[22]. These oral sensors are integrated with resonant coils without battery operation and are able to detect salivary bacteria at the single-cell level in vitro. Such biosensing concepts could also be further extended to monitoring of other salivary biomarkers. Currently, oral biosensing devices have been further miniaturized into removable "cavity sensor" devices for the detection of salivary glucose on mouthguards mounted on the wearer's teeth. The sensor is based on a GOX-modified polyethylene terephthalate surface that is seamlessly integrated with a wireless transmitter on a customized monolithic mouthguard. This configuration enables telemetry of salivary glucose in artificial saliva over a relevant physiological range (5-1, 000 µM) and further characterizes the device by connecting the phantom jaw (simulating the human oral cavity) to the salivary flow system.

Research and Application of Flexible Electronics and Devices in Gas Sensor

Zhong Ma et. al. tried to develop a nanostructured conductive polymer-based gas sensor with a sensitivity of up to $\Delta R/R0 = 225\%$ for 5 ppm NH_3 and an improved sensitivity of 46% and 17% for 5 ppm putrescine and cortisone, respectively, which was never reported[23]. Gas sensors play a key role as sensitive switches, and the degree of spoilage of meat can be read using smartphones when the concentration of biogenic amines exceeds a preset threshold. Jong-Seon Kim et. al. developed a high-performance chemoresistance with adjustable signal response and high sensitivity to VOC groups by using molybdenum disulfide (MoS_2) and by coupling thiolated ligands (MUA) to the MoS_2 surface, which successfully enhanced MoS_2 ground performance and opened up

new prospects for versatile sensor arrays[24]. Alexander F. Smith et al. found that bioelectronic ammonia sensors made from protein nanowires harvested from the microorganism Geobacter sulfurreducens, respond sensitively to a wide range of concentrations of ammonia (10 to 106 ppb) and can cover related fields of industrial, environmental, and biomedical applications. The sensor also exhibits high selectivity for ammonia compared to water and other common gases found in human respiration[25].

Research and Application of Flexible Electronics and Devices in Humidity Sensor

Congcong Zhu et. al. proposed a new humidity sensor based on multi-space laser-induced graphene electrodes that has good electrical properties and high mechanical stability, showing high sensitivity, stability, reliability, and short response/recovery time in a wide test range of 11% to 97% relative humidity, and has potential applications in the field of wearable and health monitoring devices[26]. Lingyi Lan et. al. proposed a convenient, effective, mass-produced method for flexible wearable humidity sensors to produce laser-induced graphene interdigitated electrodes (LIG-IDE) using laser direct writing technology, improving the complex and expensive problem of traditional method preparation. The humidity sensor prepared by the new method has low hysteresis, high sensitivity and good stability, and can be used in a variety of fields, such as non-contact humidity sensing and human respiration monitoring[27].

The above studies show that flexible electronics and devices have a wide range of research and great application potential in wearable biosensors for health care monitoring. At present, although the introduction of biosensing platforms into the

5

commercial market is slower than expected, wearable biosensors for blood glucose monitoring are expected to account for a large share of the market. With the rapid growth of research reports on flexible electronics and devices, their applications in various types of sensors also have broader prospects.

1.2 Research and development of laser-induced graphene (LIG)

Due to its excellent chemical and physical properties, graphene has been extensively researched in fundamental science and device applications[28]. With higher available area, the synthesis of three-dimensional (3D) graphene foams is generally more widely engineered than pristine two-dimensional (2D) forms. Graphene foams have been successfully prepared through a variety of routes, including wet-chemical method[29, 30] and chemical vapor deposition (CVD) [31, 32]. For these approaches, a large amount of strong acid and oxidant or high temperature furnace and high purity gas are usually required[29-32].

Graphene and the discovery of laser-induced graphene

In early practice, lasers were used to replace the original heat source, thereby simulating the CVD process, that is, dissolving carbon in a metal catalyst under heating and then forming a graphene structure on the metal surface, a process that usually requires assisted cooling. However, this method requires the use of metal catalysts and etching processes, which are costly and time-consuming. In 2011, Ajayan reported the direct patterning of graphene electronics on hydrated GO films. In this method, GO films are first prepared by vacuum filtration, and then the irradiated area is converted into graphene using a CO_2 laser printer, and the process is usually called laser reduced

graphene oxide (LRGO). Although this process avoids the use of metal catalysts and uses hydrated GO as the ionic conductive layer, it is often convenient to use GO as the carbon source. GO membranes are thermally unstable and may affect the reproducibility and stability of devices produced by this process.

Although laser irradiation of polymer films to prepare amorphous carbon can date back to the 1980s, the direct formation of graphene materials on polymer by direct laser scribing was seldom reported until laser-induced graphene (LIG) was prepared polyimide (PI) films by direct writing using an infrared CO_2 laser instrument under conventional environmental conditions in 2014[33].

Due to the in-site synthesis method, LIG is well attached on the PI surface, providing a 3D surface-bound foam structure with flexibility and conductivity. The preparation process of LIG does not require a furnace or precise control of air pressure, and the corresponding pattern can be made directly with graphene foam on the device surface under specific device conditions, so it is more advantageous than traditional graphene preparation methods, especially in the preparation of graphene films. Molecular dynamics simulations of the phase transition using the ReaxFF potential indicates that the high pressure and high temperature conditions imposed by transient laser heating are the main reasons for the formation of graphene structure[34], and a critical energy of 5.5 J cm^{-2} is required to initiate the transformation. In general, higher energy will form an aperture in graphene foam.

Research and Development of Laser-Induced Graphene (LIG)

Due to the unique advantages of LIG in 3D graphene synthesis, many research

groups around the world are using laser-induced methods to fabricate graphene-foam-based devices. With the optimization of laser conditions, the conversion of numerous carbon precursors into LIGs and even the fabrication of graphene foam devices using 3D printing has now been achieved. Recent studies have shown that the structure of the LIG can be designed by adjusting laser parameters and substrates. The laser parameters have an important influence on the final structure of the LIG. When the pulse density is 1000 pulses/inch (PPI) × 1000 lines/inch (LPI) and the pulse diameter is 60 mm, each pulse overlaps, and the target position laser is emitted for many times to produce the porous structure. However, when the pulse density is reduced to 500 PPI × 500 LPI, a fibrous structure is formed when each pulse has a minimal overlap, known as LIG fiber (LIGF). At the same image density, the LIG aperture was found to also increase with the laser power from 2.4 W to 5.4 W. In general, Raman spectra showed that the graphene produced at higher laser power had better graphene quality. Changing the substrate can also adjust the structure of the LIG. In 2017, Ye used wood as precursors and patterned LIG on the surface of wood[35]. Wood is mainly composed of lignin, cellulose, and hemicellulose. Upon laser induction, the lignin fraction will be converted to LIG and cellulose and hemicellulose will be ablated. Different mesoporous LIG structures can be achieved using the natural skeleton of different wood and the control of laser parameters.

Heteroatom doping or forming composites with graphene is an effective way to improve the material properties.

Composites can combine the characteristics of additive and graphene and may

produce synergistic effects. Therefore, since the report of LIG in 2014, there are many works on the adjustment study of LIG compositions. In Lin's work in 2014, since PI is a nitrogen-containing polymer, LIG prepared by PI is usually nitrogen-doped. Laser power can control the content of dopants, and higher power has been found to reduce the nitrogen content. The composition of the substrate can also be changed by the formation of composite materials, for example, in 2015, Peng prepared a polymer composite composed of PI and boric acid and used it as a substrate to form boron doped LIG[36]. Ki-Ho Nam et.al. used a continuous-wave infrared laser to directly produce micropatterns of heteroatom-doped porous graphene on polyimides with different backbones and effectively used heteroatom-doped (n-doped, F-doped, and S-doped) ground graphene to fabricate conductive microelectrodes. The resistivity of F-doped and N-doped geo-graphene is able to be achieved below ~13 Ω/sq by modulating the laser flux, which shows superior performance in electrochemical sensing of dopamine[37].

Studies on the conversion of generic substrates to LIG.

Based on the previous research, most of polymers cannot form LIG under laser irradiation except PI and polyetherimide (PEI). Subsequent studies have found that some other polymers such as phenolic resins are also suitable for LIG synthesis, but the quality of the synthesized graphene is usually poor and can be improved by controlling the anaerobic laser environment. Inspired by wood conversion, Chyan and Ye developed a protocol that can convert many carbon materials into LIG under conventional environmental conditions[38]. In general, laser-induced synthesis can be

performed directly for polymers with high thermal stability, such as PI, PSU, and PES[33, 39]. For the polymers with moderate thermal stability, such as PEI, cross-linked polystyrene and phenolic resin, it is feasible to use focused laser beam to perform multiple laser shots or use defocused laser to perform equivalent laser shots. Through defocusing, the laser spots overlap, and it is feasible to effectively perform multiple laser shots on surface. In such a process, the substrate will first be converted to amorphous carbon and then further converted to LIG with improved graphene quality after the second and third laser shots. Raman spectra are shown for stepwise conversion of PEI. For less thermostable polymers, such as cellulosic materials, conversion can be achieved by pretreatment of the substrate or carbonized substrate surface with a flame retardant prior to laser induction. This effectively avoids the drastic interaction between the substrate and oxygen during lasing. By following the principle, a large number of materials have been successfully converted into LIGs with good graphene quality.

The development of LIG has been at an alarming rate, and it is currently invested by many countries worldwide in improving the morphology of graphene foams and increasing their practicability.

1.3 Research and application of metal oxides by laser irradiation

Metal oxides (MOs) are significant for the development of scientific and technology due to various unique physicochemical properties. MOs are composed of at least one metal cation and one oxygen anion can be synthesized with different crystal structures, showing the electronic properties from insulators to semiconductors to conductors[40, 41], and has been widely employed in many fields such as electrolyte

capacitors, ferroelectric memory, piezoelectric sensors, photocatalysis, gas sensors, transparent screens, infrared detectors, fuel cells, and solar cells. Thin films and nanostructures of MOs have become an essential part in the design of functional devices. These oxide films and nanostructures have traditionally been synthesized using deposition methods of liquids, gases, ionized vapor, or plasma[40, 41]. Wet chemical processes, such as sol-gel techniques and metal-organic deposition (MOD), are commonly used for the growth of MO films. Co-precipitation and hydrothermal methods are more commonly used for the synthesis of nanostructured MOs. In all these methods, heat treatment or annealing of solution-derived precursor or nanostructures is usually necessary. Heat treatment of MO films and nanostructures is usually performed in ovens or furnaces in the temperature range of 300 – 1000 °C. Since the sample size is much smaller than the heating volume, almost all the energy is used to raise and lower the temperature of the substrate and the furnace itself. In addition, heat treatment processes based on conventional heating methods cannot induce spatially resolved thermal effects and require physical separation of thin films or nanostructures from electronic circuits. These problems limit the direct integration of MO films or nanostructures into complementary metal oxide-semiconductor (CMOS) fabrication processes.

As an alternative to conventional heat treatment, laser irradiation offers a potential solution to the above problems and enables highly compatible on-chip integration of MO films and nanostructures. This technique is mainly based on the photothermal effect induced by the focused laser, which can remotely generate a confined temperature

field at a desired location and is highly controllable[42]. Several laser process parameters such as laser intensity, pulse width, and scan rate can be varied to achieve the desired thermal effect. This process is characterized by significant rapid and local thermal effects, allowing precise control of material properties. The heating and cooling rates of laser irradiation are orders of magnitude higher than the rates of conventional annealing and rapid thermal annealing (RTA), enabling rapid fabrication of materials with minimal energy loss. Since laser-induced heat can be restricted to specific regions in the in-plane and thickness directions, films and nanostructures can be selectively annealed without any thermal interference to the underlying substrate and adjacent structures. In addition, the use of a laser with sufficient efficiency (defined as the ratio of the light output power and the input electrical power) significantly reduces the energy required for heat treatment[43, 44].

Laser systems operating in continuous wave (CW) or pulsed mode in the ultraviolet (UV), visible (vis), and infrared (IR) ranges have been used to customize the properties/functions of metal oxides. Laser irradiation of various MO films and nanostructures has been used in dielectric[45, 46], ferroelectric, piezoelectric and multiferroic devices, photocatalytic, gas sensors, transparent conductors, field-effect transistors, solar cells and thermistors. In addition, laser irradiation techniques have been used to deal with complex nanostructures, such as site-specific growth of nanowires (NWs) and nanorods (NRs), spatial patterning of nanocrystals and NWs, fabrication of nanosheets and clustered nanostructures.

1.4 Advantages and applications of molybdenum dioxide

Molybdenum dioxide (MoO_2) is an attractive transition metal oxide because of its low metal resistivity, high melting point and high chemical stability. Thanks to its efficient charge transport characteristics, molybdenum dioxide has a broad application prospect in the fields of catalysis, sensing, electrochromic display, recording medium, electrochemical supercapacitor and field emission. In addition, MoO_2 can also be used in soft robotics driven by light due to its high photothermal efficiency. However, to our knowledge, applications of MoO_2 are mainly limited to the field of energy storage and photothermal conversion. Moreover, its application in wearable devices still far exceeds the degree of development. In addition, MoO_2 is mainly synthesized by hydrothermal or calcination of the reported work, which requires harsh conditions, such as high temperature and pressure, limiting its expedient application in wearable devices. In order to take full advantage of these ideal properties of MoO_2 and explore suitable methods for in situ synthesis of highly conductive MoO_2 on flexible substrates, it will be promising for application in wearable devices.

1.5 Advantages and applications of porous SEBS materials

According to the latest research, the multiscale pores of porous polystyrene-segmented poly (ethylene-ran-butene)-segmented polystyrene (SEBS) can effectively backscatter sunlight and minimize endotherm, while heat dissipation can be maintained because the pore size is too small to reflect infrared radiation in the human body. In addition to superior passive cooling capabilities, multiscale porous SEBS substrates exhibit many other characteristics required for skin-wearable electronics, including waterproofness, high air permeability, recyclability, low elastic modulus, low mass

density, high extensibility, and conformability. Firstly, compared with non-porous SEBS, multiscale porous SEBS exhibits high hydrophobicity due to increased surface roughness due to porous structure and shows excellent waterproof ability in form-preserving contact with skin, which is further confirmed by on-body device testing in water. Secondly, due to interconnected layered pores, porous SEBS shows a higher water vapor permeability (WVTR) ($0.0206 \text{ g} \cdot \text{cm}^{-2} \cdot \text{h}^{-1}$), about 69 times higher than nonporous SEBS of the same thickness, and comparable to the recently developed passively cooled nanoPE fabric ($0.023 \text{ g} \cdot \text{cm}^{-2} \cdot \text{h}^{-1}$)[47]. High WVTR can accelerate sweat evaporation to improve user comfort as well as minimize the inflammatory response caused by sweat accumulation. Thirdly, the introduction of a porous structure in the SEBS substrate can reduce mass occupation and also create sufficient local voids to reduce the effective elastic modulus. Therefore, the porous SEBS substrate is ultra-soft and lightweight. Its modulus (~ 0.2 mPa) and mass density (~ 0.25 g/cm^3) are comparable to those of epidermis (modulus, 0.14 to 0.6 mPa; density, ~ 1.05 g/cm^3) and smaller than those measured by nonporous SEBS (modulus, ~ 1.1 mPa; density, ~ 0.89 g/cm^3). The low modulus of elasticity avoids skin irritation, improves user comfort, and facilitates formable contact with the skin. The low mass density allows lightweight skin electronics to ease the physical constraints imposed on the human body. In addition, the multiscale porous SEBS matrix is highly scalable ($\sim 600\%$) and elastic.

1.6 Application and potential of actuator and soft robots

Robots have been widely used in many fields, but traditional robots and actuators have strong structural rigidity and poor environmental adaptability. To overcome the

above shortcomings, researchers draw inspiration from nature and create more flexible and multifunctional soft robots and actuators. The main materials of soft robots and actuators are soft materials, which theoretically have infinite degrees of freedom and can change the morphology at will within a certain limit. At present, the typical software robots include Meshworm robots developed by MIT and Harvard University, which can use SMA to simulate earthworm peristalsis and resist strong impact[47]; biomimetic octopus under development by LASCHI, Italy; soft robots integrating the glowing artificial skin and inflatable structure of Cornell University; and biomimetic manta ray robotic fish developed by Virginia University, which are driven by ion exchange polymeric metal materials and have the ability to switch different movement modes. The structure of such soft robots is generally compared with worm and cephalopod designs, while the driving mode mostly uses shape memory alloy drive or chemical drive.

In recent years, researchers still look to nature and expect to develop soft actuators that can utilize the energy of the natural environment. For example, inspired by sunflower tracking the sun, pine cones releasing mature seeds in a dry environment and the phototactic movement of flies, soft actuators that produce mechanical deformation under external energy stimulation have been greatly developed and have received great attention in the fields of soft robots, artificial muscles, smart wearable clothing, and MEMS. Actuators driven by light have become one of the attractive actuators in all kinds of soft drives due to their advantages of no contact, concise control and rich light source.

1.7 Our work

In order to meet the requirements of high conductivity of current path and base electrode and good biocompatibility, high sensitivity and stability of monitoring sensor for skin wearable devices, we developed direct laser scribing MoO_2 (DLS-MoO_2) high conductive trace on breathable, flexible and chemical stability SEBS substrate. And by following electrode modifications and functionalization, we manufactured multifunctional flexible wearable epidermal devices. Assembled by temperature sensor, sweat sensor, electrophysiological sensors, alcohol sensor, NH_3 sensor, humidity sensor and UV sensor, the achieved SEBS-MoO_2 based can monitor information like electrocardiogram (ECG), electroencephalogram (EEG), humidity, temperature, UV, NH_3 and alcohol concentration. Furthermore, photo actuates soft robotics based on the photothermal transformation of MoO_2 have also been developed. The DLS-MoO_2 presented in this work open a novel view for the fabrication of flexible epidermal electronics.

Chapter 2. Material Preparation and Characterizations

2.1 Materials and reagents

Molybdenum (V) chloride ($MoCl_5$), ethanol, isopropyl alcohol (IPA), iron chloride hexahydrate ($FeCl_3 \cdot 6H_2O$), hydrochloric acid (HCl), sulfuric acid (H_2SO_4), buffer solutions (pH=3.0, 4.0, 5.0, 6.0, 7.0, and 8.0), ammonium hydroxide, aniline were purchased from Fisher Scientific., ammonium persulfate, iron (III) p-toluene sulfonate hexahydrate, potassium permanganate ($KMnO_4$), phosphoric acid (H_3PO_4), graphite flakes and tungsten diselenide (WSe_2) nanoflakes were purchased from Sigma-Aldrich. ZnO nanowire was purchased from ACS Material. Graphene oxide was prepared as literature reported. All chemicals were used as received.

2.2 Fabrication of porous SEBS substrates

The SEBS substrates were prepared based on our previous work. Briefly, 6 g commercial SEBS powders (H1062; Asahi Kasei) were dissolved in 100 mL chloroform to obtain the SEBS solution. Then, the as prepared SEBS solution was mixed with 40 mL isopropyl alcohol followed by sonication for 10 min. After that, the resulting solution was drop-cast on aluminum foil. After drying under ambient conditions, the porous SEBS substrates were acquired.

2.3 Direct laser scribing conductive materials on porous SEBS substrates

As laser can provide the local and precisely controlled condition of high temperature and high pressure, it can be served as an efficient method to conduct precise, low-cost and versatile materials fabrication. Herein, we employed CO_2 laser (VLS2.30

universal laser system, wavelength: 10.6 μm, beam size: ≈120 μm, pulse duration: ≈14

μs, maximum power: 30 W, maximum scanning speed: ≈23 in. s^{-1}) with the beam of

10.6 μm to direct writing conductive MoO_2 patterns on porous soft SEBS (**Figure 2.3.1**).

Firstly, $MoCl_5$ was dissolved in water as a concentration of 5 M, then the $MoCl_5$

solution was further diluted to 1 M using ethanol. Then the diluted $MoCl_5$ solution was

spray coated on the O_2 plasma etching system treated SEBS substrates at about 90 °C

on hot plate. Next, the treated SEBS substrates were patterned by a CO_2 laser with the

setting of 7% of the maximum power and 15% of the maximum scanning speed.

Subsequently, the laser patterned substrates were soaked in DI water until the precursor

in unpatterned area washed away followed by drying in air temperature.
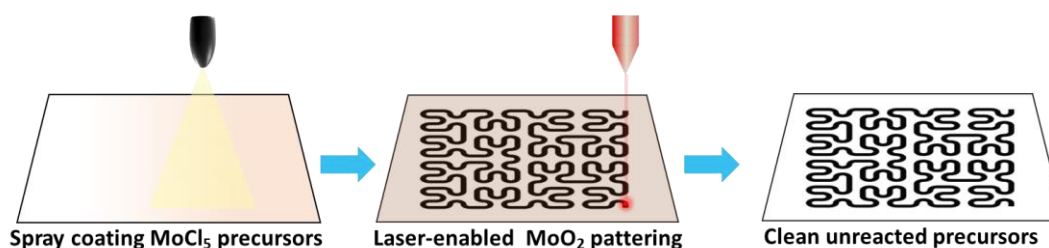
Figure 2.3.1 Schematic illustration of the fabrication process of the Direct Laser Scribing MoO_2 devices

To investigate influence of laser power and precursor amount on the morphologies

of the obtained materials, scan electron microscope (SEM) images are conducted. The

results display that at a fixed power scan speed (15 % of the max scan speed) and

precursor amount of 2 mL in 4cm×4cm square (125 μL cm^{-2}), with the increasing of

power (from 6%-9% of max power) (**Figure 2.3.2**), the attained material presented
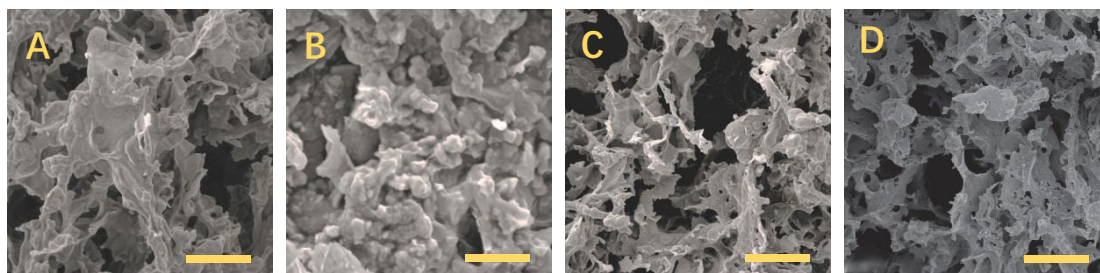
more porous structures.

Figure 2.3.2 SEM images of materials on SEBS substrates under various laser power A) 6%, B)7%, C) 8%, and D) 9% with same laser speed of 15% and precursor amount of 2 mL (Scale bar 10 μm)

While as laser power is fixed as 7% of the max power and the deposition amounts of precursor are growing, the obtained materials manifest a bulk structure (**Figure 2.3.3**).
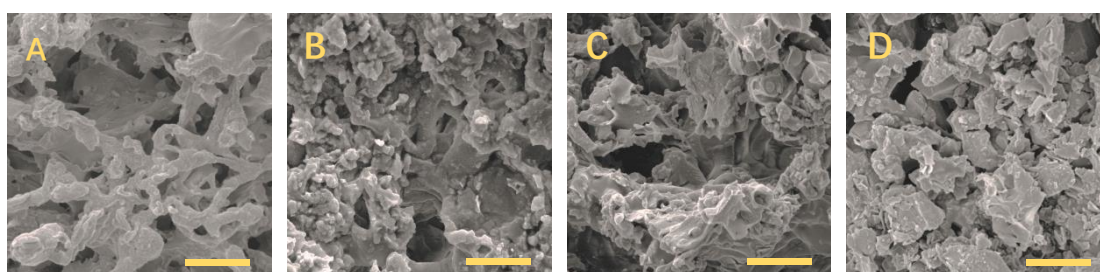

Figure 2.3.3 SEM images of materials on SEBS substrates with various precursor amount of A) 1 mL, B) 2 mL, C) 3 mL, D) 4 mL under same laser power of 7% and laser speed of 15% (Scale bar 10 μm)

For the application of flexible wearable devices, the conductivity of materials play a vital role. So as to achieve the MoO_2 with best conductivity, the sheet resistance change of the laser-scribed materials along with the precursor amount and laser power at the set scan speed of 15% are investigated. As shown in **Figure 2.3.4**, compared with the amount deposited on SEBS, laser power has more obvious influence on the sheet resistance of the materials. It should be ascribed that at a lower power, the precursor cannot transform to MoO_2 successfully, while at higher power, there are also some by-products and the high temperature will lead to mass loss of material. At the modified parameters of 7% power and precursor solution of 2 mL (125 μL cm^{-2}), we obtain the material with the lowest sheet resistance of 7 Ω/sq, which is exceptional among the
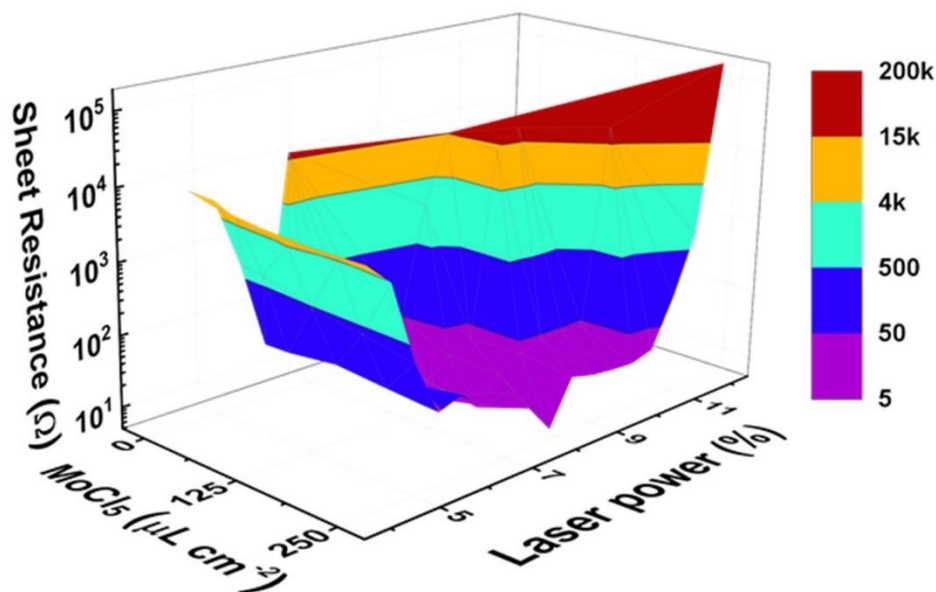
laser-scribed materials.

Figure 2.3.4 Sheet resistance of the materials controlled by laser power and precursor amount

From the cross-section image of the material on SEBS (**Figure2.3.5A**) and correspond EDS mapping of Mo (**Figure 2.3.5B**) illuminate that the thickness of materials on SEBS is about 50 μm.
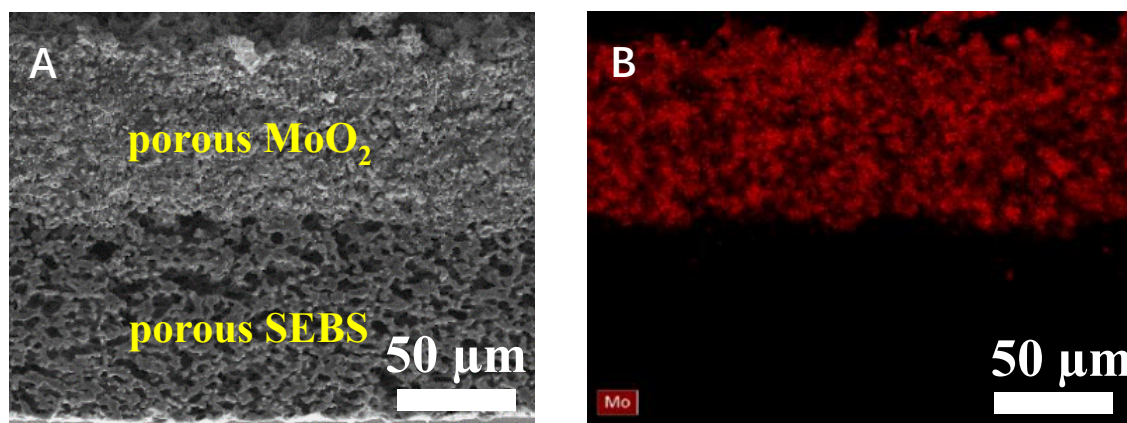

Figure 2.3.5 A) Cross-section image of porous MoO₂ on porous SEBS substrate, B) EDS mapping of Mo on cross-section

2.4 Characterization

To further demonstrate the crystal structure of the obtained materials, XRD patterns of the achieved materials are obtained, as exhibited in **Figure 2.4.1**, several

diffraction peaks at about 26.1º, 36.8º, 36.9º, 41.4º, 49.7º, 53.7º, 60.8º and 66.6º can be found for all the materials, corresponding to the (-1 1 1), (2 0 0), (1 1 1), (2 1 0), (-3 0 1), (-2 2 2), (-3 1 3) and (-4 0 2) lattice planes of monoclinic MoO_2 in the space group of P21 (JCPDS no. 32-0671).
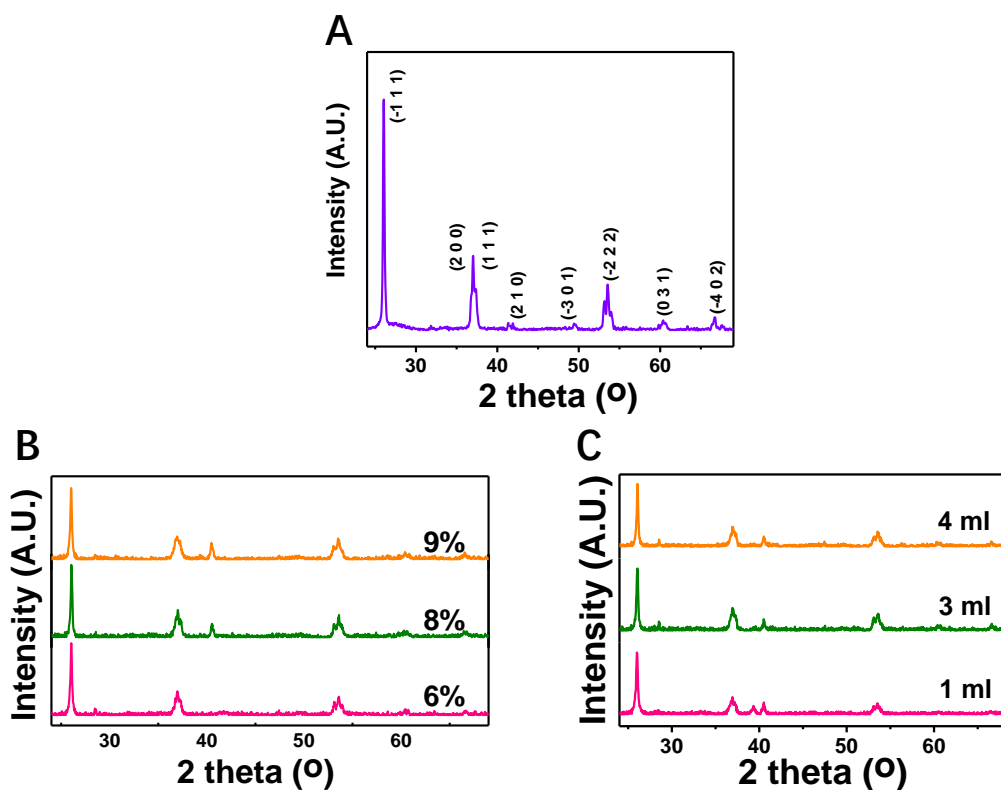

Figure 2.4.1 XRD patterns of A) materials on SEBS substrates under laser power of 7% with laser speed of 15% and precursor amount of 2 mL, B) materials on SEBS substrates under various laser power (6%-9%) with same laser speed of 15% and precursor amount of 2 mL, C) materials on SEBS substrates with various precursor amount (from 1 mL to 4 mL) under same laser power of 7% and laser speed of 15%

From the Raman spectra (**Figure 2.4.2A and B**), several peaks located at about 128, 201, 228, 361, 495, 571 and 744 cm^{-1} are presented, attributed to the stretching vibrations of Mo-O bond.
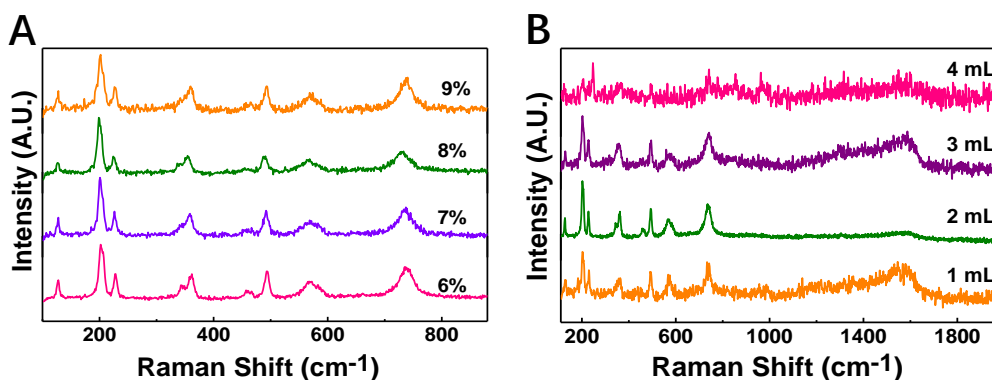
Figure 2.4.2 Raman spectra of A) materials on SEBS substrates under various laser power (6%-9%) with same laser speed of 15% and precursor amount of 2 mL, B) materials on SEBS substrates with various precursor amount (from 1 mL to 4 mL) under same laser power of 7% and laser speed of 15%

Further structure characterizations are conducted by transmission electron microscope (TEM) and flake structures are found (**Figure 2.4.3A**). Besides, from the high resolution TEM (HRTEM) image (**Figure 2.4.3B**), obvious lattice fringes with the interlayer distances of 0.24 nm，0.34 nm and 0.24 nm can be found, corresponding to the (1 1 1), (-1 1 1) and (2 0 0) lattice planes of MoO_2 crystalline. Additionally, Fast Fourier Transform (FFT) pattern (**Figure 2.4.3C**) of the HRTEM shows a clear single crystalline electron diffraction pattern and can be indexed to MoO_2 [0 -1 1] the zone Axis based on the monoclinic structure (JCPDS no. 32-0671). Additionally, the simulated electron diffraction pattern (**Figure 2.4.3D**) using the CrystalMaker^{TM} is in well agreement with the experimental FFT pattern, further confirming the MoO_2 phase.
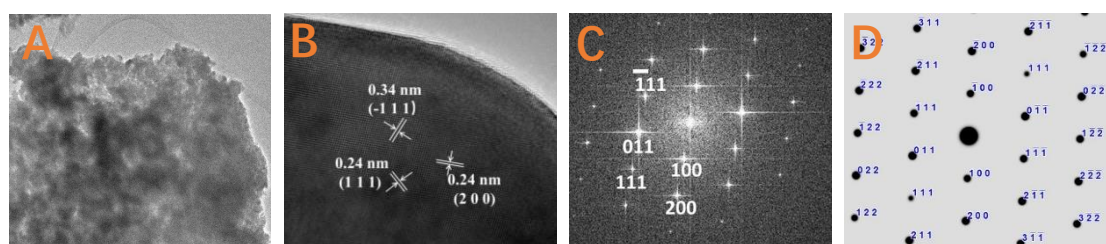

Figure 2.4.3 A) TEM image of DLS-MoO_2, B) HRTEM image of DLS-MoO_2, C) FFT pattern of the HRTEM, D) Simulated electron diffraction pattern

The X-ray diffraction (XRD) patterns were obtained using a Philips X'Pert

22

Materials Research diffractmeter equipped with a CuKα radiation source. Raman spectra were conducted on a Renishaw Raman microscope. FEI Quanta 600F Environmental Scan electronic microscope (SEM) and FEI Tecnai F30 G2 Twin Transmission Electron Microscope (TEM) were employed to collect morphologies images and crystals analysis. EDS data were obtained by Bruker Quantax 200 EDS (SSD).

2.5 Fabrication of MoO$_2$ on different substrates.

Besides the successful fabrication of laser direct scribing MoO$_2$ on flexible porous SEBS substrates, the adaptability of this method is also demonstrated by preparing MoO$_2$ on different substrates including non-porous SEBS film, PI films, glass and even hair. As the XRD (**Figure 2.5.1A**) and Raman (**Figure 2.5.1B**) results exposed, MoO$_2$ are achieved on all of those substrates. An SEM image of MoO$_2$ on hair after DLS is presented as **Figure 2.5.2**. The change of the I-V curves of hair before and after the writing of MoO$_2$ exhibited in **Figure 2.5.3** can also provide further validation.
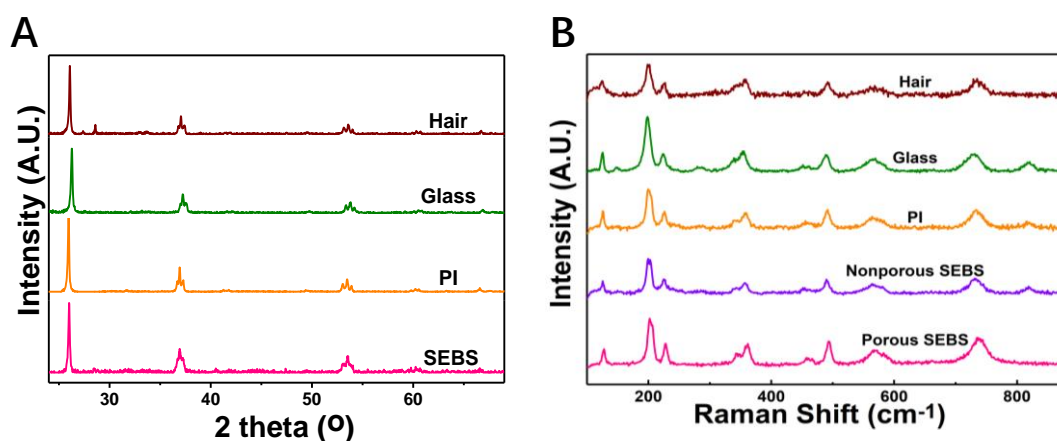

Figure 2.5.1 A) XRD patterns of DLS-MoO$_2$ on different substrates, B) Raman spectra of DLS-MoO$_2$ on different substrates
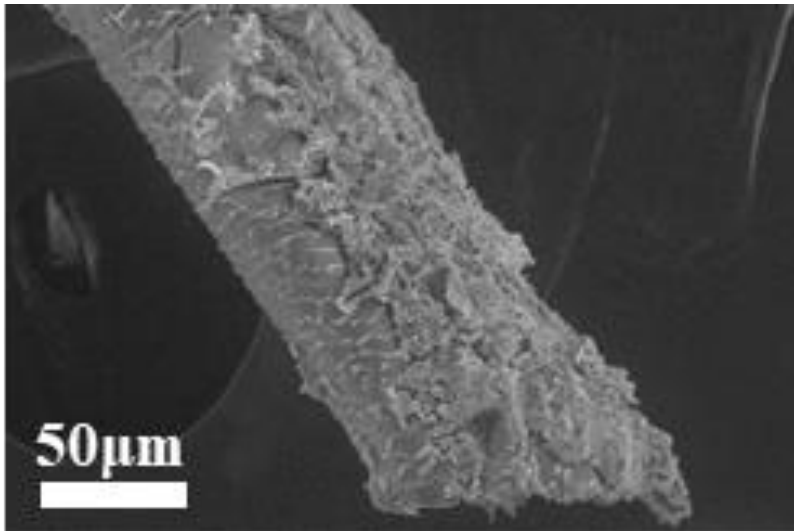
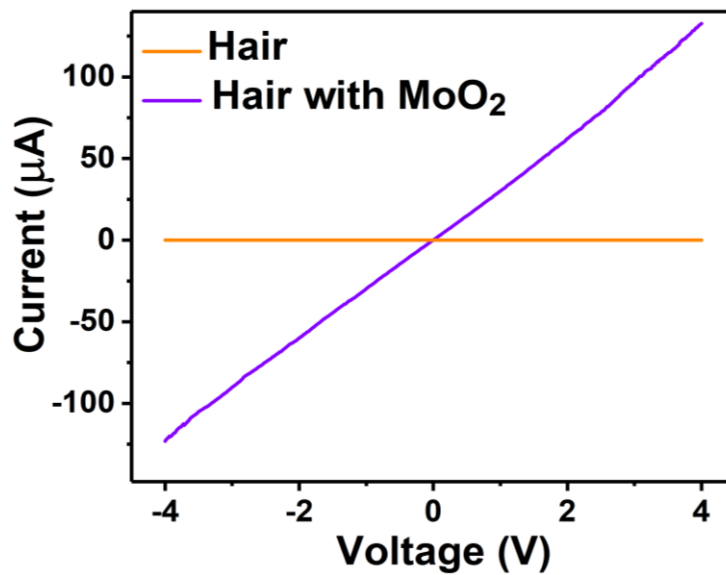**Figure 2.5.2 SEM image of DLS-MoO₂ on hair**

Figure 2.5.3 I-V curves of hair before and after the DLS of MoO₂

Based on those results, we believe that the laser direct scribing MoO$_2$ process has negligible influence on the substrate and to demonstrate, we collect SEM images of MoO$_2$ based on glass and PI substrates (**Figure 2.5.4**) and no obvious substrates change is discovered.
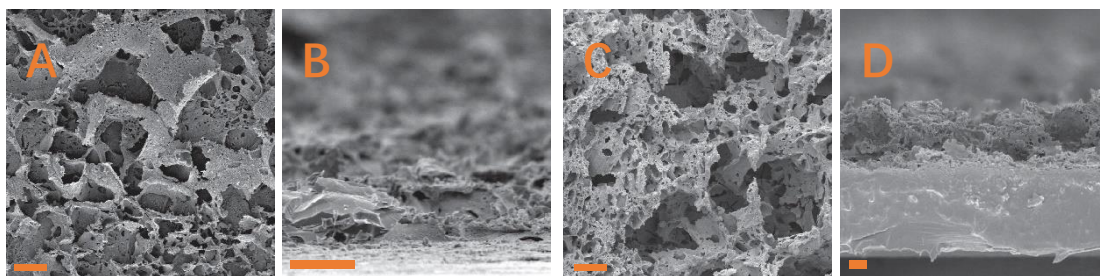
Figure 2.5.4 SEM images of DLS-MoO$_2$ on glass (A, B) and PI (C, D) substrates (Scale bar 10 µm)

To further prove this point, we conduct the SEM images of original porous SEBS substrates (**Figure 2.5.5A**), after laser direct scribing MoO$_2$ process (**Figure 2.5.5B**) and the obtained MoO$_2$ on the surface are removed by several hours' ultrasonic treatment (**Figure 2.5.5C**). As contrast experiments, the SEM images of porous SEBS after DLS are also carried out (**Figure 2.5.5D**).
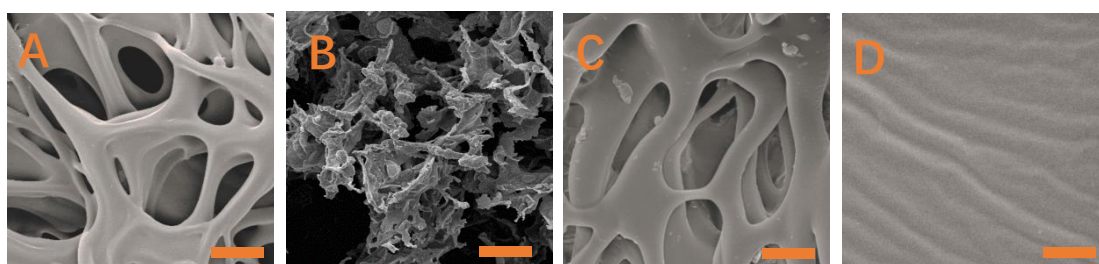

Figure 2.5.5 SEM images of A) porous SEBS, B) laser scribed MoO$_2$, C) SEBS after removing prepared materials, D) direct laser scribing on porous SEBS

The results indicate that the SEBS substrates after direct laser scribing MoO$_2$ process display the similar porous structures with the original porous SEBS, while the porous structures of direct laser scribed SEBS are fully damaged, which demonstrates that precursor on the surface of substrates can protect the substrates from thermal damage by absorbing most of the energy produced by laser.

2.6 Mechanical performances

The mechanical stability is a critical factor for the wearable devices. The electrical

resistance changes of the direct laser scribing MoO_2 pattern on porous SEBS substrates

(**Figure 2.5.1**) are tested and the results are displayed in **Figure 2.5.2**.
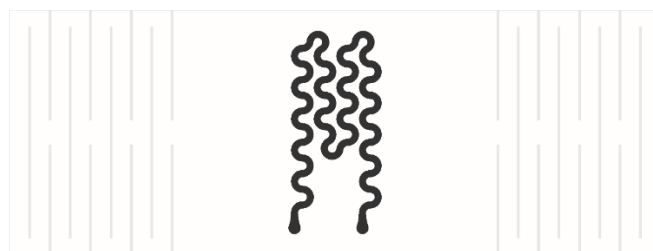

Figure 2.5.1 Design layout of MoO_2 on porous SEBS substrates with kirigami cuts
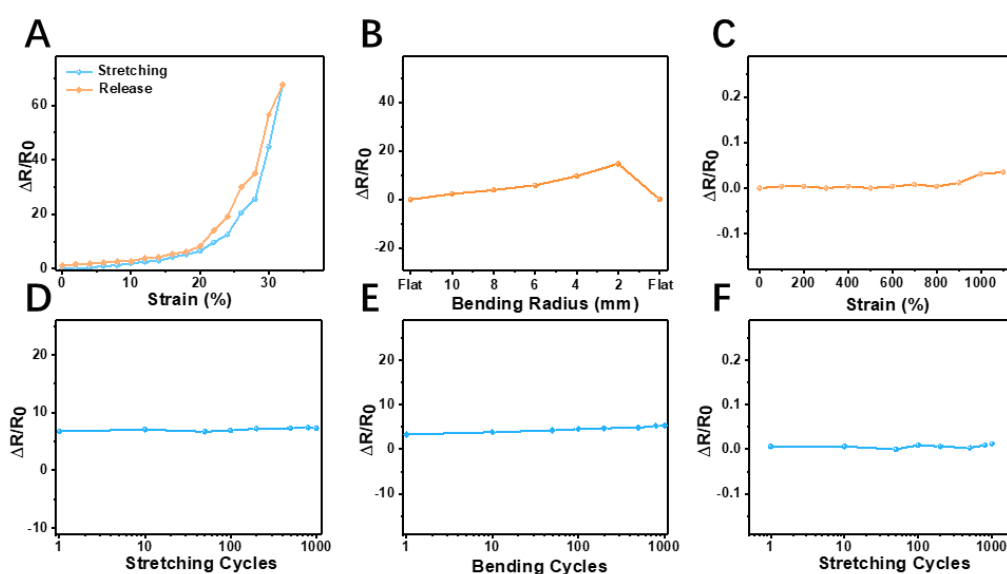

Figure 2.5.2 Characterizations of electromechanical properties. A) Electrical-resistance variation in a typical
stretch/release cycle, B) at different bending radii, C) the related electrical-resistance variation at different tensile strains
with kirigami cuts applied, D) as a function of stretching cycles, E) as a function of bending cycles for a bending radius of
8 mm, F) as a function of stretching cycles with kirigami cuts applied

Besides, by applying kirigami cuts, the stretchability performances are obviously

enhanced. The electrical resistance of laser writing MoO_2 pattern on porous SEBS show

no noticeable change under up to ~500% tensile strain.

Mechanical performances were conducted on Mark-10 ESM303 tensile tester.

Chapter 3. Multifunctional Sensors Based on DLS-MoO_2

3.1 Multifunctional flexible sensors

As a breathable, flexible substrate with chemical stability, SEBS is employed with MoO$_2$, a fascinating transition metal oxide with low metal resistivity, high melting point and high chemical stability. Combining the characteristics of porous SEBS and DLS-MoO$_2$, we fabricated a material promising in flexible electronics and soft robotics. By following electrode modifications and functionalization, we manufactured multifunctional flexible sensors.

3.2 Design of multifunctional flexible sensor

The physical and biochemical sensors included in our multifunctional patches are electrophysiological sensors, humidity sensors, UV sensors, alcohol sensors, and NH$_3$ sensors, as illustrated in **Figure 3.2.1**. The sensors employ breathable, stretchable and chemically stable porous SEBS as substrates. On the bottom side of the patch, electrophysiological sensors and temperature sensor are directed acquired by direct laser induced MoO$_2$ patterns. On the top side of the illustration, four pairs of MoO$_2$ interdigitated electrodes (IDEs) are fabricated by direct laser writing and after drop cast of as-obtained WSe$_2$ solution, graphene solution, ZnO solution and p-toluene sulfonate hexahydrate doped polyaniline (PTS-PANI) solution. Alcohol sensors, humidity sensors, UV sensors and NH$_3$ sensors are fabricated respectively. To realize the high-fidelity signals recording, here we explore gelatin-dopamine based highly adhesive glue to guarantee the conformal contact between skin and the multifunctional patches. After adding the glue, the patch can be well attached to forearm and presented a high adhesiveness. The multifunctional sensors are used for monitoring the daily activities of humans, such as the food spoilage detection, UV, humidity monitoring, concentration

monitoring of biochemical after corresponding food intake and the physical change

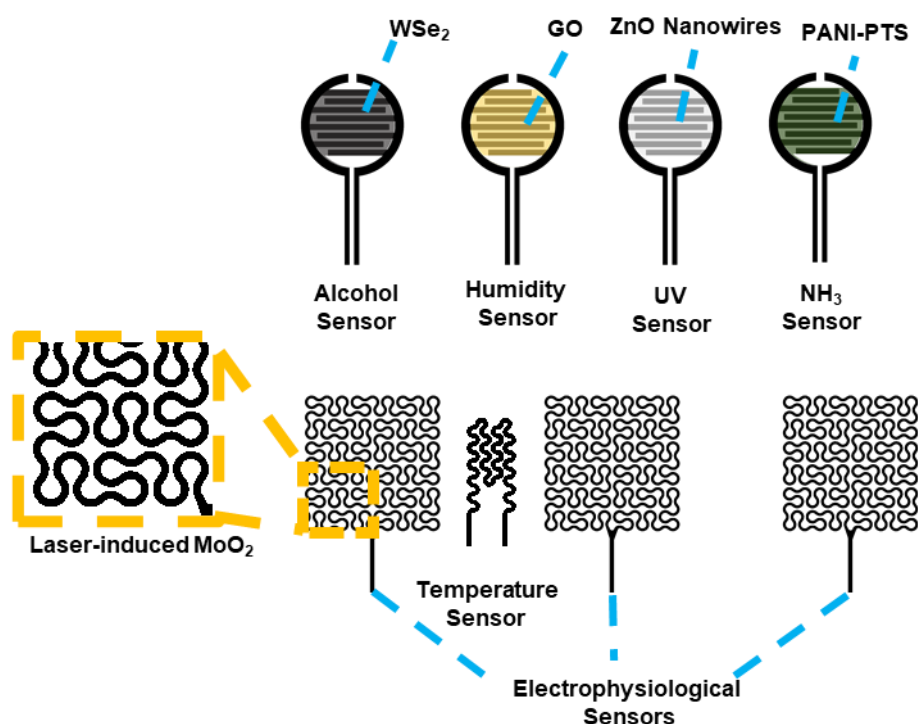including EEG, heart rate and breathe alcohol concentration after alcohol intake.

Figure 3.2.1 Schematic illustration of multifunctional sensors

3.3 Electrophysiology sensors

3.3.1 Introduction

Electrophysiology is the study of the electrical properties of biological cells and

tissues and involves measuring changes in voltage or electric current[48]. These

measurements span a wide range of length scales from single ion channel proteins

through neurons to whole organs such as the heart. Common electrophysiological

techniques include electrocardiology (ECG), which provides detailed information on

the ventricles and atria for cardiac disease[49]; electroencephalography (EEG), which

measures electrical activities in the brain for studies of sleep apnea[50], epilepsy[51],

and other neural disorders[49]; and electromyography (EMG), which provides

information on nerve and muscle health[49, 52].

For electrophysiology sensors, impedance and electrical impedance are two significant performances. Improving the adhesion of the active sensing material to the substrate can then improve the robustness and reliability of the mechanical sensor[53]. The recording quality depends largely on the electrical impedance of the electrode-skin-body interface, since skin-interface electrodes in wearable sensors convert naturally occurring, time-dependent ion currents in the human body into measurable electrical signals [53].

3.3.2 Method

Electrophysiological sensors are directed acquired by direct laser induced MoO_2 patterns.

Electrophysiological signals recording and electronic stimulation were conducted on PowerLab T26 (AD Instruments). The resistances, impedances and capacity were measured using LCR Meter (IM3523, HIOKI) and Dual Channel SourceMeter (2604B, Keithley Instruments).

3.3.3 Results

Since the porous SEBS substrates are not stick and can't contact with skin intimately, which may cause poor electrophysiological signals recording. To overcome this problem, we explore an adhesive reagent by mixing gelatin (0.05 g mL^{-1} in water) and dopamine (10% in water) with a specific ratio of 3:1. As presented in **Figure 3.3.1A and B**, strong skin adhesion was demonstrated and the measured peel force can reach to 145 N m^{-1} when trace amount of the mixture are coated on the SEBS.
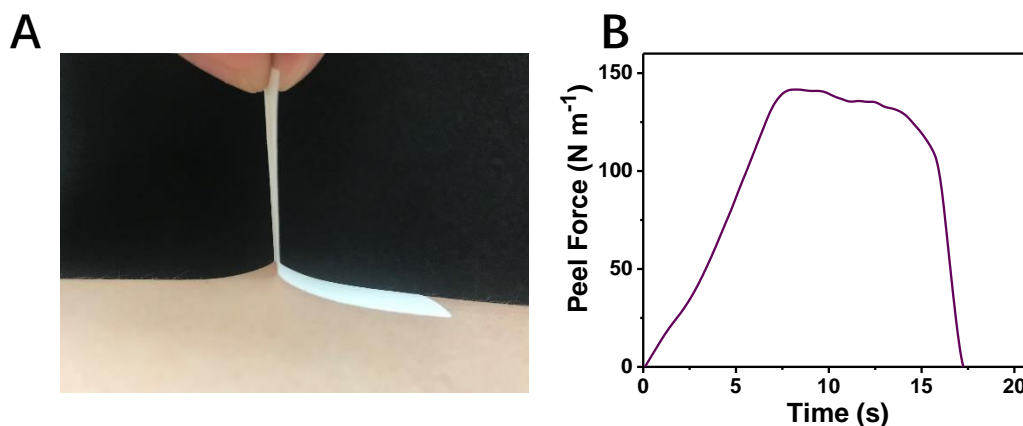
Figure 3.3.1 A) Optical image presenting strong skin adhesion of SEBS substrates coated with adhesive reagent in peel force test, B) Peel force test of SEBS substrates coated with adhesive reagent from the human forearm

Real-time, high-fidelity and long-term recording of electrophysiological sensor related to human activities, like ECG, EEG and electromyogram (EMG) are critical in health monitoring and physiological state. The DLS-MoO$_2$ epidermal electronics on porous SEBS exhibited outstanding performances as shown in **Figure 3.3.2**, the skin contact impedance of the device is about 34 KΩ at 100 Hz, which is lower than commercial Ag/AgCl gel electrodes.
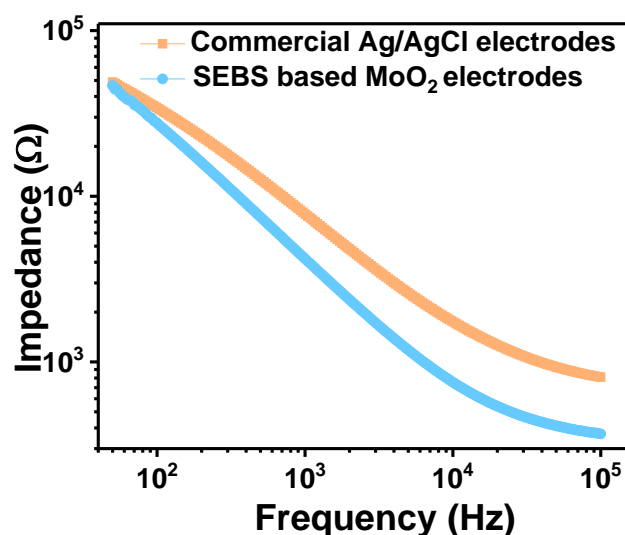

Figure 3.3.2 log$_{10}$(Impedance) as a function of log$_{10}$(Frequency) of commercial Ag/AgCl gel electrodes and SEBS based MoO$_2$ electrodes

The devices are glued to the volunteer's chest for a long-time ECG recording, and

signals with distinguishable P-wave, QRS complex and T-wave are achieved (**Figure 3.3.3A and B**). High quantity signals obtained after 2, 5, 8, 12, and 24 h are also obtained, indicating the good stability of the device. Since the R peak amplitudes in QRS complex decrease the expiration and increase during the inspiration, the respiration rate can be calculated according to the obtained ECG signals. From 80s ECG signals shown in **Figure 3.3.4**, the calculation respiration results from ECG are agree well with the results by visual counting (**Figure 3.3.5A**). Also, the instantaneous heart rates calculated by R-R intervals from our devices are fully coincide with the commercial Ag/AgCl electrodes (**Figure 3.3.5B**).
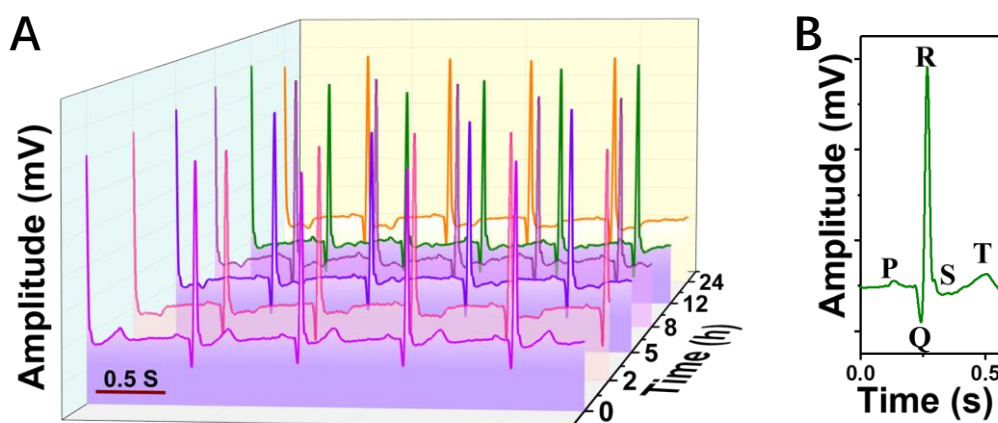

Figure 3.3.3 A) Long-term monitoring of ECG using DLS-MoO$_2$ electrodes for 1 day, B) Magnified ECG signal indicating clear P-wave, QRS complex, and T-wave
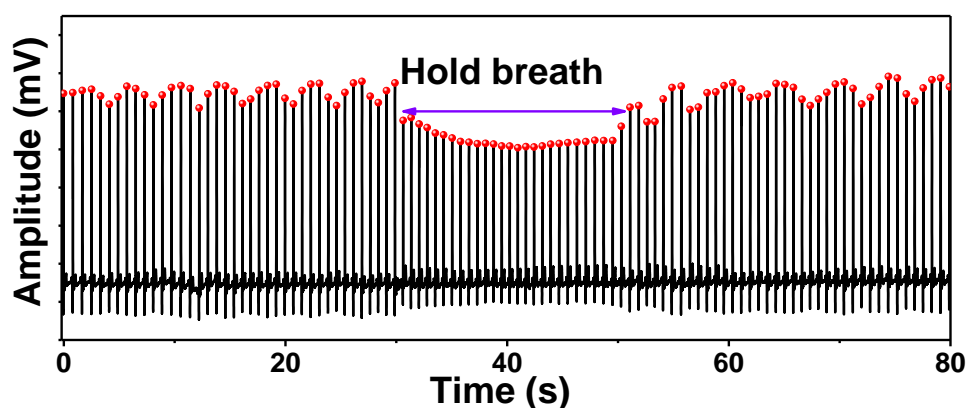
Figure 3.3.4 Dynamic amplitude responses of the R peaks in the ECG signals while the volunteer held the breath for ~20s
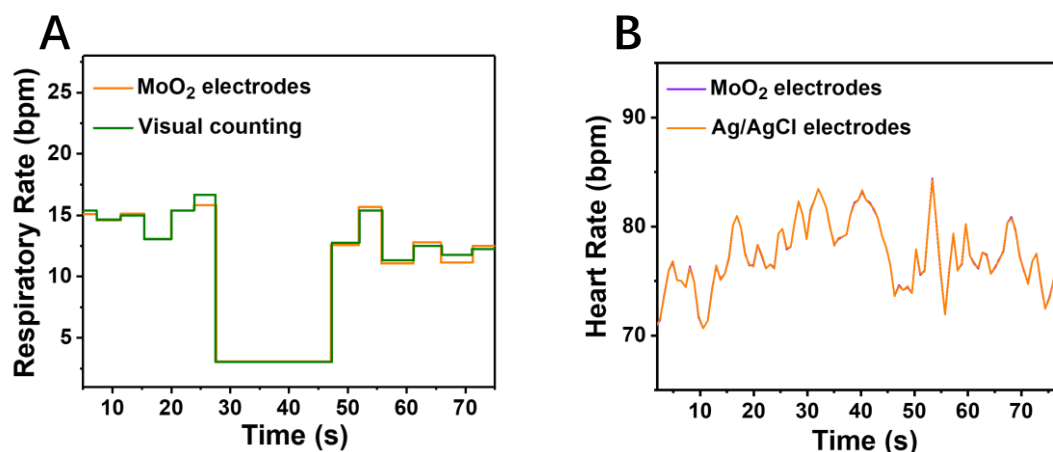

Figure 3.3.5 A) Respiratory rates determined by the R peak amplitude variations in Figure 3.3.4 and visual counting by a physician. B) Comparisons of instantaneous heart rates determined from the R-to-R peak intervals in the ECG signals recorded with MoO$_2$ on-skin sensors and conventional Ag/AgCl electrodes.

High quality EMG signals are also collected from the DLS-MoO$_2$ epidermal electronics on porous SEBS. When the devices are applied on the forearm (flexor carpi radialis muscle) of a volunteer, the EMG signals produced by wrist flexion (**Figure 3.3.6A**) and even a finger flexion (**Figure 3.3.6B**) can be clearly detected. Furthermore, when we use DLS-MoO$_2$ as electrodes and a monophasic square pulses of 2 mA with pulse duration of 50 ms (**Figure 3.3.7A**) are applied to the forearms of a volunteer to conduct electrical stimulations, high-amplitude EMG signals are also detected (**Figure 3.3.7B**).
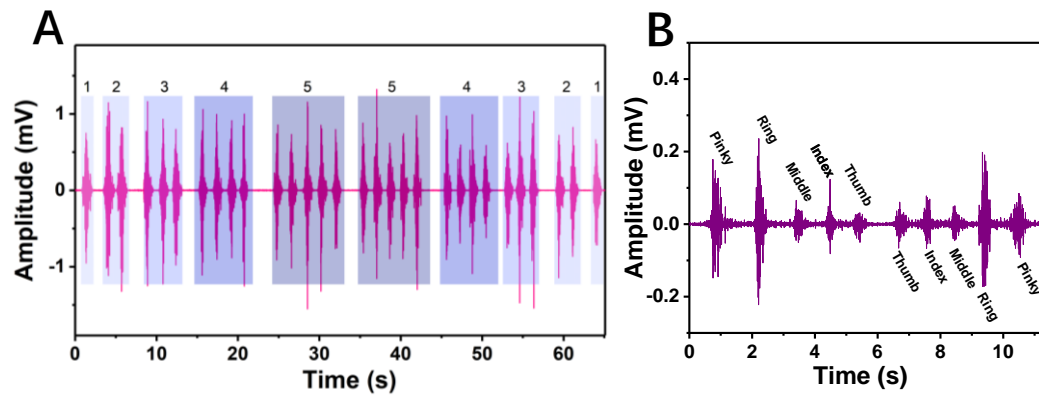
Figure 3.3.6 A) EMG signals produced by wrist flexion, B) by finger flexion
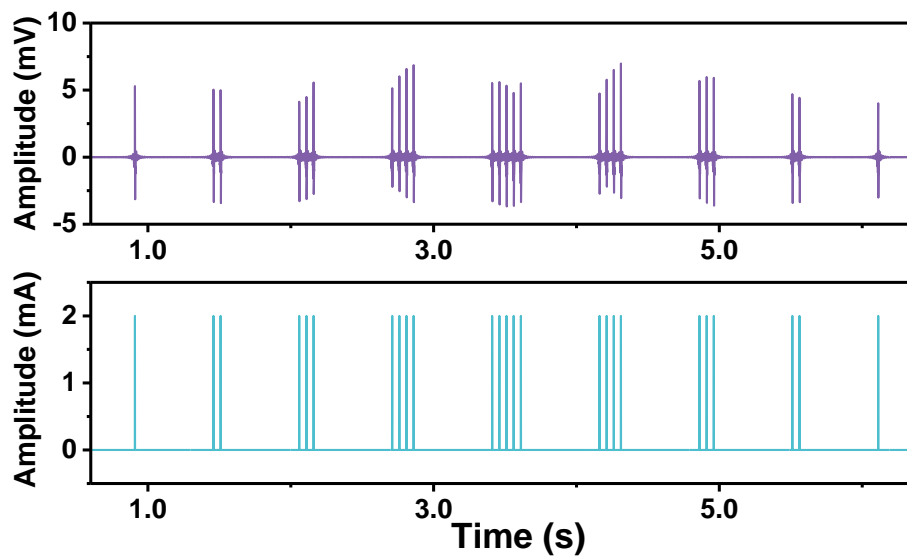
Figure 3.3.7 Recorded EMG signals (Top) during electrical stimulations (Bottom)

3.4 Temperature sensor

3.4.1 Introduction

Temperature reflects the balance between production and dissipate of heat. Flexible temperature sensors are primary sensors used for temperature monitoring. To obtain real-time and accurate information of temperature, different flexible temperature sensors are developed according to the principle of flexible resistance temperature detector (FRTC), flexible thermocouple, flexible thermistor and flexible thermochromic, showing great potential in energy conversion and storage[54]. Herein,

we designed a temperature sensor based on DLS-MoO$_2$ thermistor.

3.4.2 Method

Temperature sensors are directed acquired by direct laser induced MoO$_2$ patterns.

Temperature calibrations were measured using thermocouples (SA1-K, OMEGA Engineering) with a thermometer (HH309A, OMEGA Engineering). Infrared images were collected by commercial thermal camera (FLIR E6).

3.4.3 Results

As reported previously, DLS-MoO$_2$ exhibits positive temperature coefficient of resistance (0.72% $^{\circ}$C^{-1}) (**Figure 3.4.1A and Figure 3.4.1B**). The temperature change of the DLS-MoO$_2$ under the shadow of infrared hot lamp are shown in **Figure 3.4.2**, the results calculated from the devices match well with that measured by thermocouple. The **Figure 3.4.3** validates that on-skin joule heating application of the DLS-MoO$_2$ when a 10 v, and even during the wrist is flexed and extended, the obtained devices can also sustain a steady temperature.
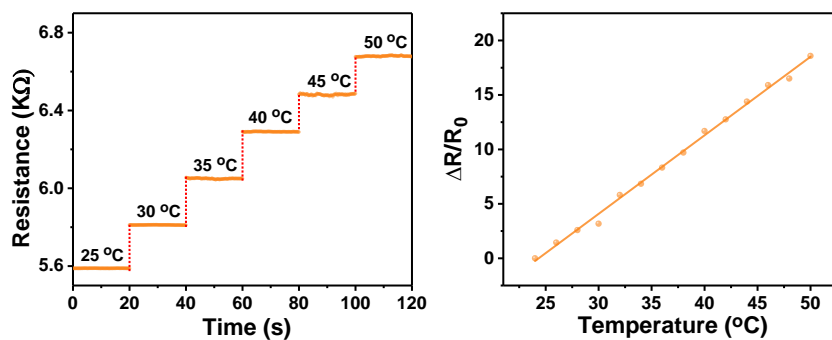
Figure 3.4.1 A) Linear relationship between resistance and temperature, B) Linear fitting of resistance variations as a function of temperature
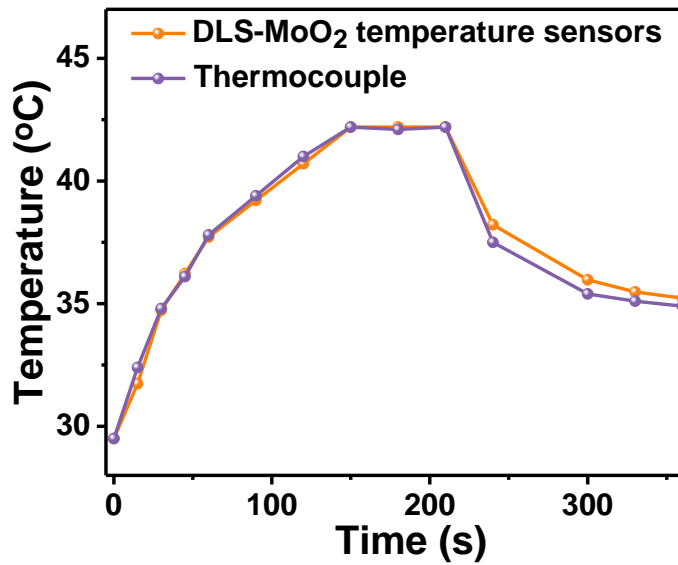
Figure 3.4.2 Calculated results of temperature change of the DLS-MoO$_2$ temperature sensor under the shadow of infrared hot lamp and the measured results from thermocouple
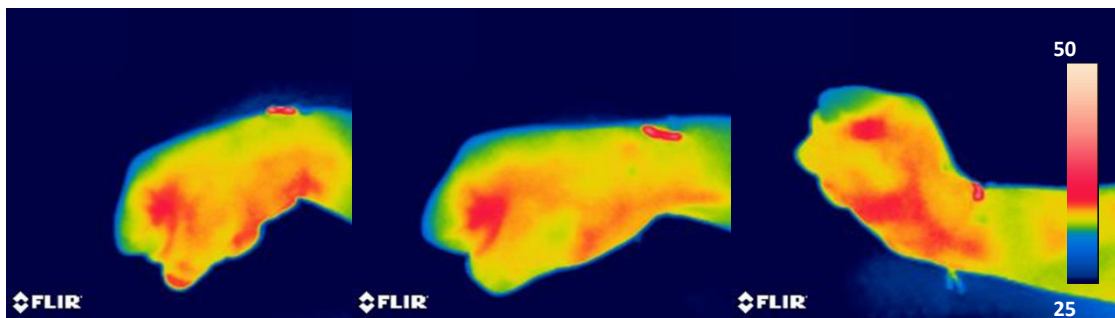
Figure 3.4.3 Thermal mapping images of DLS-MoO$_2$ on-skin joule heating application

3.5 UV sensor

3.5.1 Introduction

Ultraviolet (UV) light provides a special benefit on the well-being of humans by killing microorganisms. However, higher exposure has been reported to cause side effects such as skin cancer, cataracts or immune system suppression. Therefore, sensors that possess the ability of efficiently detecting UV signals have attracted huge attention[55-57]. Amongst various materials for UV sensors, the zinc oxide (ZnO)

nanostructure is considered as one of the most promising candidates due to its incredible electrical, optical, biomedical, energetic and preparing properties[58]. Here we fabricated UV sensors based on ZnO nanowires drop cast on DLS-MoO$_2$ substrate.

3.5.2 Method

UV sensors were modified by adding 100 μL ZnO nanowires solution (3 mg mL^{-1} in water) to specific interdigital electrodes (IDEs) area.

A UV Lamp and UV meter were used to produce UV light with specific intensity and the intensity was adjusted by the changing of distance between the lamp and sensors. The current was recorded continuously under a voltage range of -2-2 V. S.

UV intensity was calibrated by UV Meter (General Tools, UV513AB, 280-400 nm).

3.5.3 Results

The performances of UV sensor are presented as figures below. The I–V curves displayed in **Figure 3.5.1A** illustrate the increasing current with the UV intensity increasing from 0 to 1000 μW cm^{-2}. The linear relationship between the current at the applied voltage of 1 V and log$_{10}$(UV) is presented in **Figure 3.5.1B**. The average sensitivity of 0.73 μA for 1 μW cm^{-2} UV increase from 100-1000 μW cm^{-2} can be achieved. The resistance change along with the time is presented in **Figure 3.5.1C**. Shown in **Figure 3.5.1D**, the sensor exhibits a high resistance of about 40 MΩ when there the UV is off while the resistance drops to about 1 MΩ when the UV is on. The UV sensors demonstrated an ultrafast response time of 1.3 s (The response time was defined as the time taken to reach 90% of the maximum resistance response after the

UV is on).
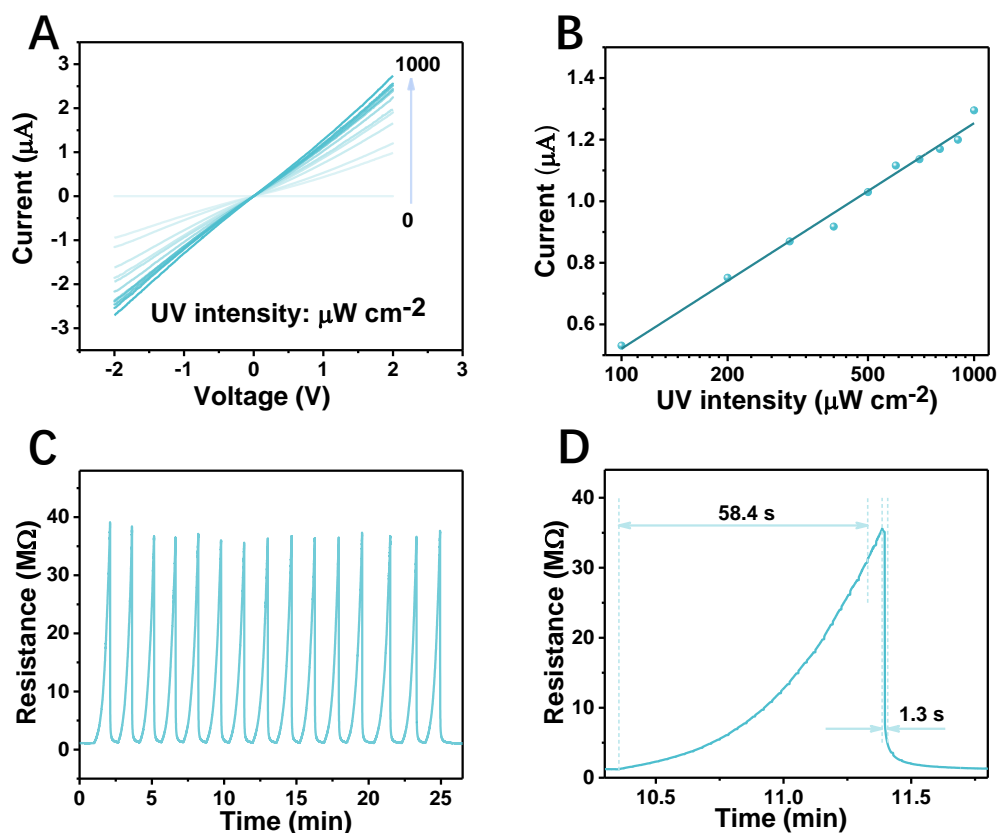
Figure 3.5.1 A) I–V curves with the UV intensity increasing from 0 to 1000 μW cm^{-2}, B) Linear relationship between the current at the applied voltage of 1 V and log$_{10}$(UV), C) Resistance change along with time, D) Ultrafast response time of 1.3 s for resistance to drop from 40 MΩ to 1 MΩ

3.6 Humidity sensor

3.6.1 Introduction

Humidity sensors are a common type of sensors in our daily life, and play a significant role in numerous application fields ranging from humidity control for various kinds of industrial processing, agricultural moisture monitoring, and medical fields to weather forecasting, indoor humidity sensing, and domestic machine controlling[59-62]. Simply, humidity sensors show the humidity by converting the amount of water molecules in the environment into a measurable signal. According to

the change of the physical parameters after interacting with water molecules, humidity sensors can be categorized into many types, such as the capacitive type, resistive type, impedance type, optic-fiber type, quartz crystal microbalance (QCM) type, surface acoustic wave (SAW) type, resonance type, and so on[59].

Capacitive humidity sensors utilize the special properties of GO materials, which are insulating, but show proton conductivity when the surfaces adsorb water molecules, with the proton conductivity being related to the water concentration in the environment. This induces the change of the capacitance[63]. Herein we fabricated humidity sensors based on ZnO nanowires drop cast on DLS-MoO$_2$ substrate.

3.6.2 Method

Humidity sensors were prepared by drop-coating 100 μL GO (3.75 % in water) to specific IDE area.

For the humidity sensor, the humidity was adjusted by injection of water vapor or adding desiccant and commercial humidity meter was employed to calibrate. The measurement of capacity was conducted on LCR meter, where the alternating current voltage was 500 mV and frequency was 100 Hz.

Humidity was recorded using a traceable hygrometer (Fisher Scientific).

3.6.3 Results

Humidity sensors are fabricated by drop cast the GO solution on the DLS-MoO$_2$ IDEs. The performances of the sensor are depicted in figures below. It can be observed that the capacitances increase significantly with the increasing relative humidity (RH) at various frequency (**Figure 3.6.1A**) and at the frequency of 100 Hz (**Figure 3.6.1B**),

RH and the $\log_{10}$(capacitances) exhibit a good linear relationship with the slope of 0.03064. The average sensitivity of 475 pF/% RH can be acquired (**Figure 3.6.1C**). We also employed the sensor to conduct respiratory detection (**Figure 3.6.1D**). When the volunteer breathe out, the sensors can capture the water vapor and the capacitance increase. Besides, when a wet finger moves closer to the sensor, obvious capacitances increasing can also be exposed (**Figure 3.6.1E and F**), demonstrating the good performances of the humidity sensors.
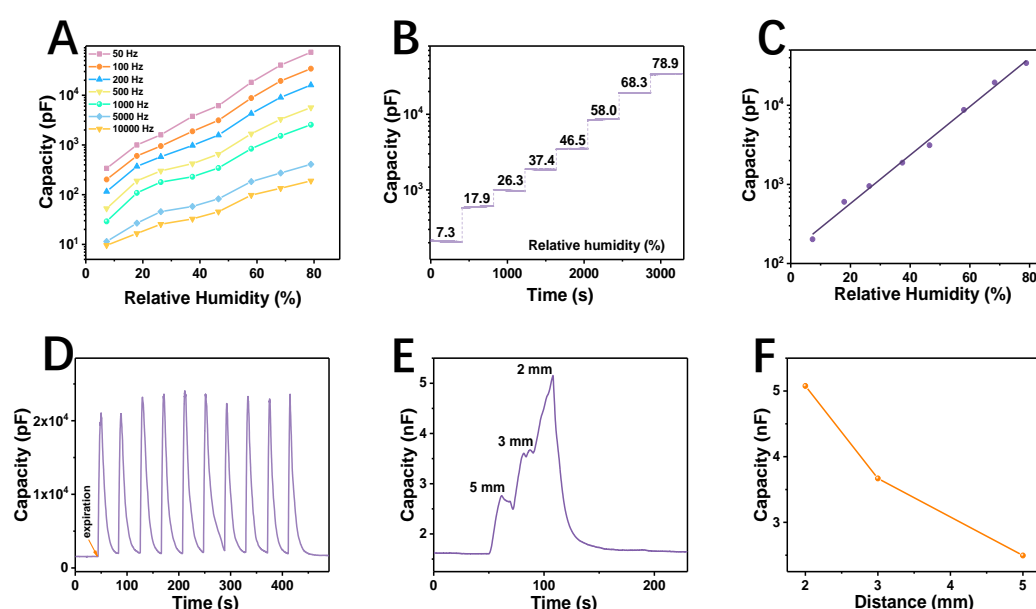
Figure 3.6.1 A) Capacitances as a function of RH at different frequency, B) log10(capacitances) as a function of time at 100 Hz, C) Linear fitting of $\log_{10}$(capacitances) as a function of RH, D) Detection of volunteer's breath in a period, E) Response of volunteer's finger moving to distance of 5 mm, 3 mm, and 2 mm to the sensor, F) Capacitances as a function of distance

3.7 Alcohol sensor

3.7.1 Introduction

Ethanol is a common organic gas and widely encountered in various areas, such as food safety, biomedicine, fuel-processing, chemical industry and traffic safety[64, 65]. Prolonged exposure to ethanol gas can cause many diseases such as lethargy,

difficulty breathing, headache and liver damage. Furthermore, ethanol is a major reason of traffic accidents over the world owing to the widespread use of ethanol as alcoholic drink. For example, the death toll from alcohol driving accounts for 31% of the total number of deaths from motor vehicle traffic accidents in US[66]. The maximum allowable ethanol concentration for Italy is 130 ppm (0.05% in blood) and 208 ppm in the US (0.08% in blood) for drivers[67].

In the transition metal disulfides (TMDs) family, tungsten selenide (WSe_2) has recently received considerable attention as an emerging nanomaterial owing to its excellent performance, such as large volume surface area ratio, excellent electrical conductivity, susceptible surface, small band gap and high stability[68]. In particular, WSe_2 exhibits an excellent response characteristic for the gas sensing at room temperature[68-71]. Herein, we fabricated alcohol sensors based on WSe_2 drop cast on DLS-MoO_2 substrate.

3.7.2 Method

Alcohol sensors were fabricated by the addition of 50μL treated WSe_2 solution (10 mg mL^{-1} in 0.5 % Nafion solution) on specific IDE area.

The calibrations of alcohol sensors are performed in a test chamber (about 14.7 L in volume). To obtain the gas with specific concentrations, a certain amount of gas was extracted from a container full of saturated alcohol vapor and injected to the test chamber. Then a fan was turned on to disperse the gas in chamber. During the test processes, either a constant direct voltage or a linear scan voltage was applied to the sensor and the current was measured continuously.

Alcohol concentrations were calibrated by BACtrack Trace Breathalyzer.

3.7.3 Results

To manufacture the alcohol gas sensor, we employ WSe_2 as active material and Nifion is added to enhance the contact between WSe_2 and IDEs. From **Figure 3.7.1A and B**, a positive increase of resistance to alcohol vapor concentration is displayed. And at the range of alcohol vapor concentrations from 100 to 1000 ppm, the resistance variations show a good linear relationship with the concentrations with the sensitivity of 1.44 %/100 ppm (**Figure 3.7.1C**). The dynamic response of the resistance variation to 10 ppm alcohol vapor is presented in **Figure 3.7.1D and Figure 3.7.1E**. Selectivity of the sensors to different molecules are also depicted in **Figure 3.7.1F**. To estimate the influence of humidity on levels on alcohol sensors, we test the resistance responses to 100 ppm alcohol at different RH performance under the RH from 20 to 100%. The response of sensor change from 19.6 % to 34.5 %.
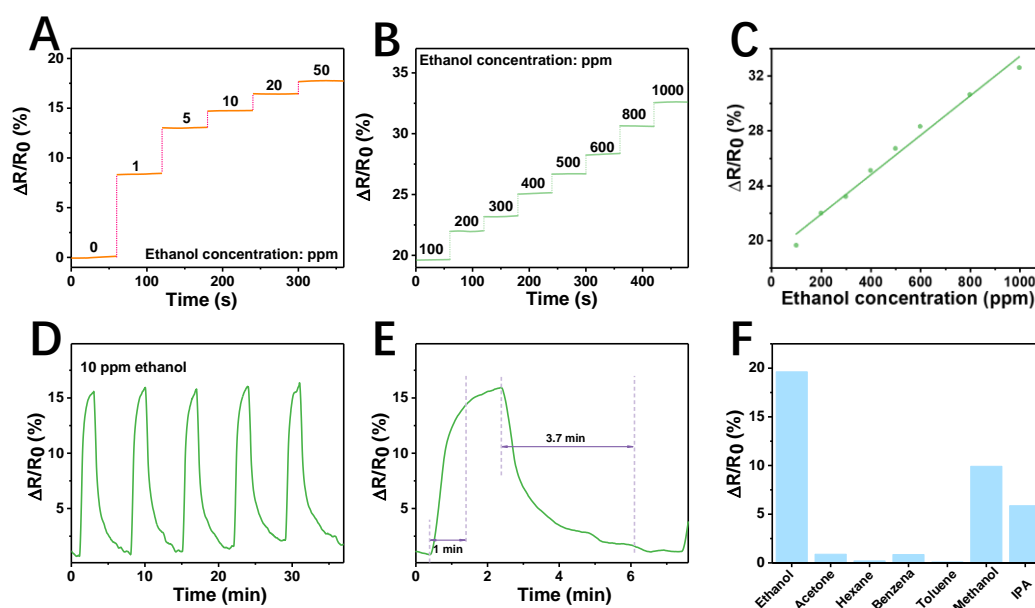

Figure 3.7.1 A) Positive increase of resistance to alcohol vapor concentration, B) Linear relationship between resistance variations and concentrations, C) Linear fitting of resistance variations as a function of ethanol concentrations, D)

41

3.8 NH$_3$ sensor

3.8.1 Introduction

As a highly toxic gas, ammonia (NH$_3$) is widely existed in the environment, such as in the air, soil and water. For humans, the skin, eyes and respiratory tract would be injured in the high concentration of NH$_3$ (ca. >300 ppm). Also, NH$_3$ is flammable at concentrations of ca. 15–28% by volume in air[72, 73]. Moreover, NH$_3$ is widely used in various applications, including refrigeration, refining, manufacturing, cleaning and nitrogenous fertilizers[74]. Iron(III) p-toluene sulfonate hexahydrate(PTS)-doped PANI shows very high sensitivity as an amine-sensing material[75]. In this research, we manufactured NH$_3$ sensors based on PTS-PANI drop cast on SEBS-MoO$_2$ substrate.

3.8.2 Method

NH$_3$ sensors were obtained by adding 100μL PTS-PANI solution (3 mg mL^{-1} in water) in corresponding IDE area.

Similar with alcohol sensors, the calibrations of NH$_3$ sensors are also performed in a custom-built vapor chamber testing system. To obtain the gas with specific concentrations, a certain amount of gas was extracted from a container full of saturated NH$_3$ gas. The resistances change along with the NH$_3$ concentrations are detected.

3.8.3 Results

To fabricate the NH$_3$ gas sensor, we employ PTS-PANI as active material. As presented in **Figure 3.8.1**, a positive increase of resistance to NH$_3$ concentration is displayed. A good linear relationship between the resistance response and NH$_3$

concentration can be found with the sensitivity of 7.3 % per ppm NH_3 at the range of 0-50 ppm (**Figure 3.8.1C**) and the sensitivity of 33% per ppm NH_3 at the range of 50-400 ppm (**Figure 3.8.1D**).
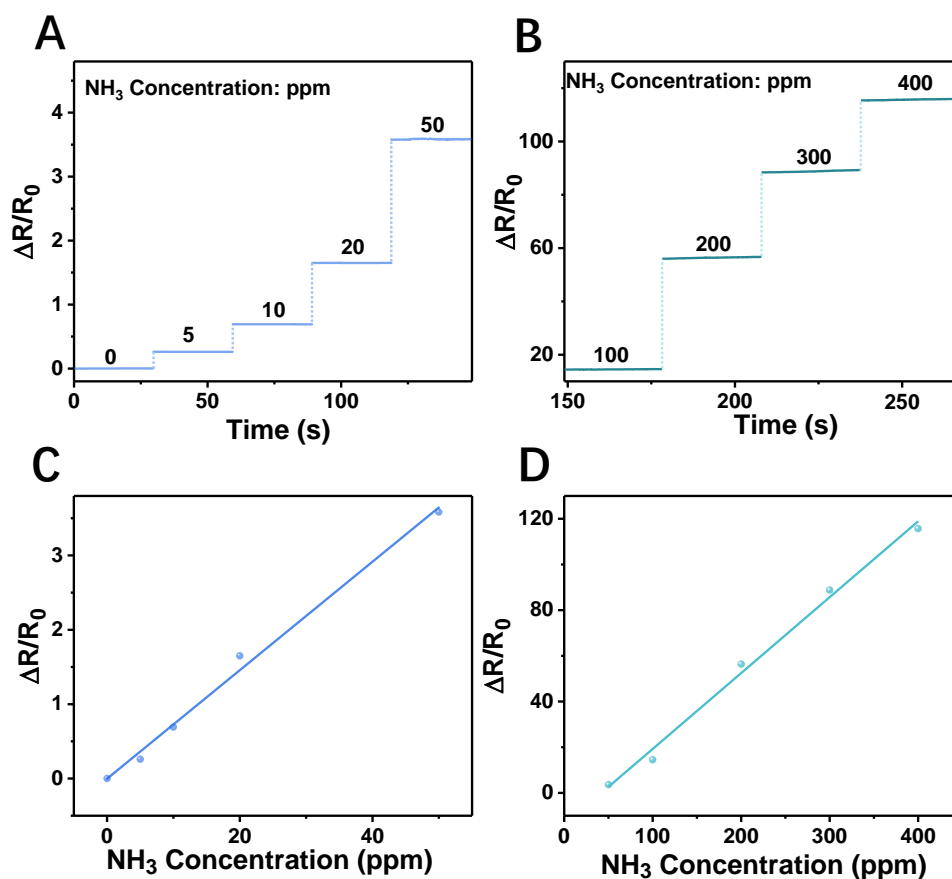

Figure 3.8.1 A) Linear relationship between resistance variations and concentrations at the range of 0 to 50 ppm, B) Linear relationship between resistance variations and concentrations at the range of 100 to 400 ppm, C) Linear fitting of resistance variations as a function of NH_3 concentrations at the range of 0 to 50 ppm, D) at the range of 100 to 400 ppm

Chapter 4. Soft Robotics

4.1 Introduction

Soft robotics have attracted broad interests, owing to its compatibility with planar fabrication techniques and applicability to a diversity of geometries and length scales. Based on the significant difference between the coefficient of thermal expansion of polyimide (PI) and Polydimethylsiloxane (PDMS), we designed and fabricated soft photothermal trilayer actuators consist of PI, DLS-MoO_2, and PDMS, with MoO_2 serving as a photothermal heater.

4.2 Method

The fabrication process of MoO_2 actuators began with the spray coating of precursor solution of $MoCl_5$ (1M in ethanol/water=4:1) on a commercial PI film (50 µm thick, Dupont). The obtained materials were then treated under direct CO_2 laser scribing under ambient conditions. The setting was fixed at 7% of the maximum power, 15% of the maximum scanning speed, and raster mode. The image density was set as 5. The pulse per inch was set as 1000. After DLS, unreacted precursors were wiped away and samples were dried in oven. Next, PDMS (Sylgard 184, Dow) is spin-coated on the sample surface and is thermally cured at ≈150 °C. The modulus of PDMS can be adjusted by controlling the weight ratio of the base elastomer and curing agent. In this research, a 10:1 ratio was employed. The PDMS thickness can be controlled by the spin-coating speed. Finally, cutting the samples into pre-designed shapes and dimensions completed the fabrication of MoO_2 actuators.

4.3 Direct laser scribed MoO₂ photothermal actuators

The actuators consist of a PI, DLS-MoO$_2$, and PDMS trilayer, as illustrated in **Figure 4.3.1**. Upon applying an infrared light source, MoO$_2$ heaters introduce temperature differences via photothermal heating. The stress caused by the significant difference in thermal expansion between PI and PDMS can induce bending deformations of the actuators toward the PI side (**Figure 4.3.1, Figure 4.3.2 and Movie 4.3.1**). Here, PDMS and PI are selected as constituent materials, largely because of their large difference in the coefficient of thermal expansion, stability at a high operation temperature, and biocompatibility. The DLS-MoO$_2$ has continuous, porous structures, which can facilitate the penetration of PDMS to strengthen the PDMS/ MoO$_2$/PI interface and enhance the cyclability of the enabled actuators. The largest bending angle accessible to MoO$_2$ actuators represents an important parameter to evaluate the actuation performance. At prescribed intensity of infrared light, the maximum bending angles of MoO$_2$ actuators can be largely affected by the modulus and thickness ratio of PDMS and PI. Here, the modulus of PI is fixed (2.5 GPa) and the modulus of PDMS can be tuned by adjusting the weight ratio of the base elastomer and curing agent. In this study, the spin-coated PDMS with a thickness of $\approx$200 μm and modulus of $\approx$2.5 MPa is majorly used for the fabrication of soft actuators and construction of 3D structures, mainly based on the tradeoff of the maximum bending angle and fabrication feasibility. Here, well-designed MoO$_2$ actuators can achieve the largest bending angle of 108° . The actuator takes about 8 s to bend from 0° to 180° and about 6 s to recover (**Figure 4.3.3A**), showing a fast response to light. The temperature change during the process of the light on and off are also researched as shown in **Figure 4.3.3B**.
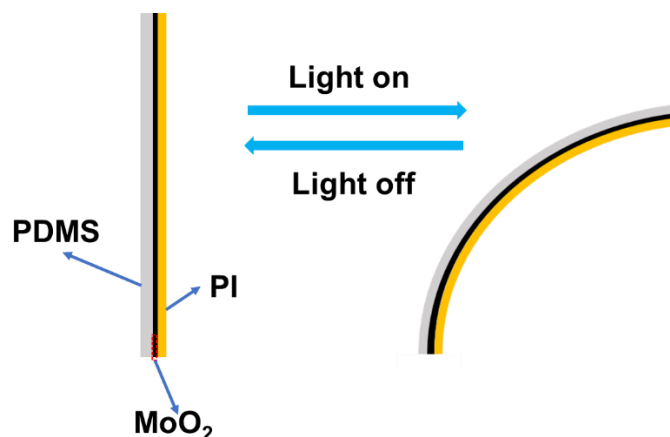
Figure 4.3.1 Schematic illustration of the MoO₂ actuator

Figure 4.3.2 Optical images of the MoO₂ bending and recovering
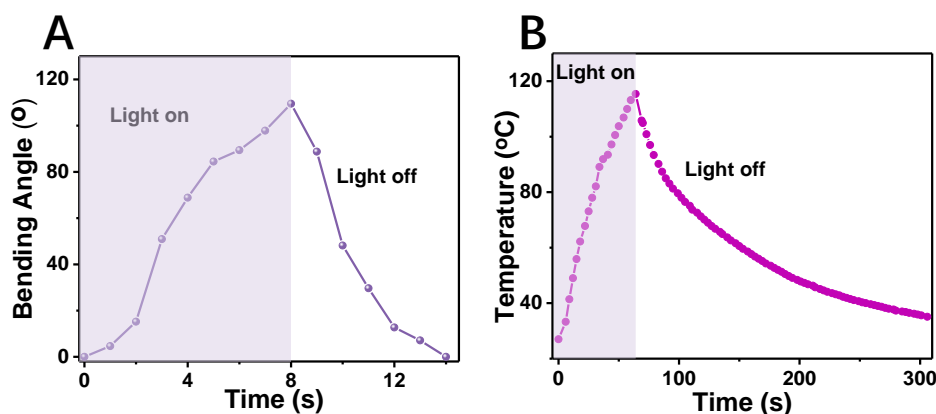
Figure 4.3.3 A) Corresponding deformation angles of the photo actuator as a function of time with the light on and off. B) Temperature variation of the photo actuator during the light on and off.

4.4 Mechanically assembled, 3D structures triggered by photothermal actuation

Incorporating ideas inspired by kirigami and origami, we have constructed 4 complicated 3D architectures with pre-determined geometries. As illustrated in **Figure 4.4.1 and Movie 4.4.1**, well-designed 2D precursors, mainly made of PI, are selectively bonded onto addressable MoO₂ actuators. Depending on the 2D precursor design, the

number of involved MoO_2 actuators and bonding sites is different. Upon photothermal actuation, well-controlled bending of MoO_2 actuators can deform 2D precursors into programmed 3D architectures.
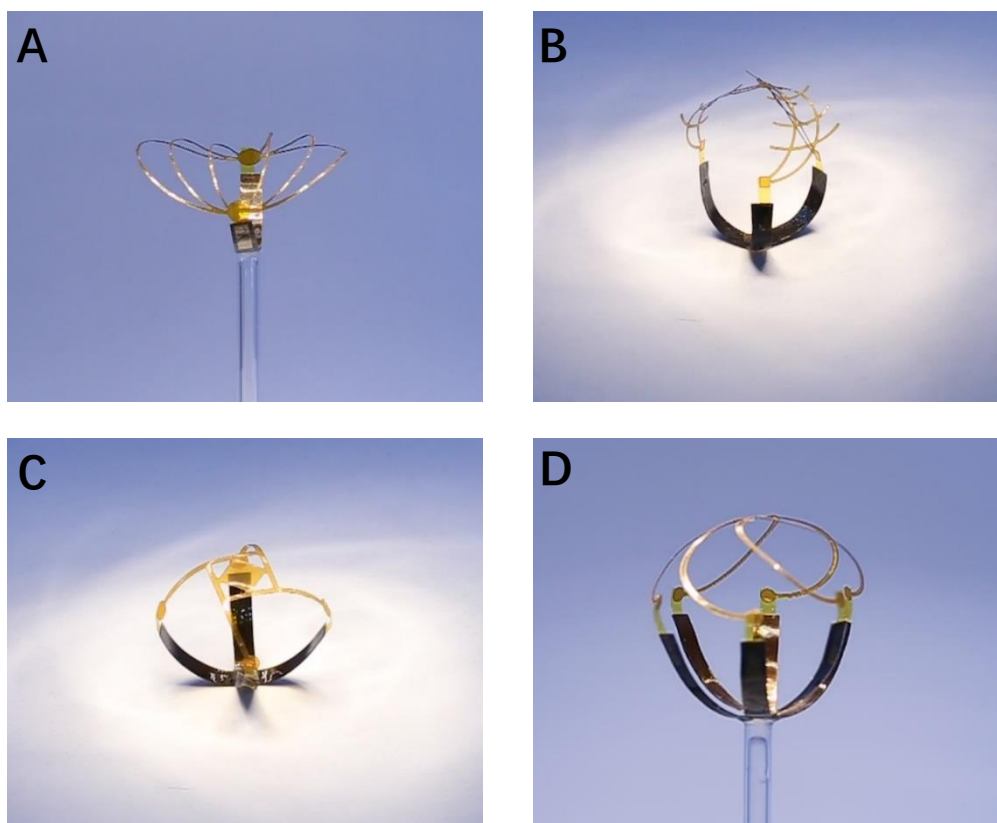
Figure 4.4.1 Optical images of four mechanically assembled 3D structures with different number of bonding sites, A) Arched Bridge, B) Thorn Basket, C) Rotated Table, D) Cage

The MoO_2 actuators can be addressed independently in the 3D assembly, which can provide the unprecedented shape morphing capability inaccessible with previous methods. As presented in **Figure 4.4.2 and Movie 4.4.2**, the flower, and umbrella can be reshaped into two distinct shapes.
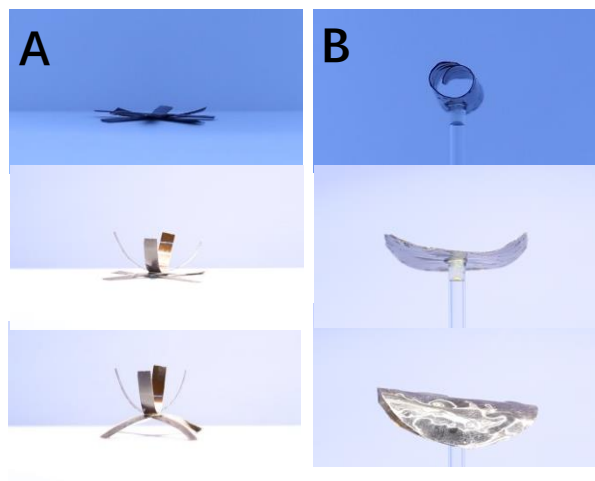
Figure 4.4.2 Optical images of 3D structures addressed independently by the MoO$_2$ actuators, A) Flower, B) Umbrella

4.5 Biomimetic self-locomotive "inchworm" robot

By taking the ambient infrared light as the energy source and simulating the crawling motion of the inchworm, we further fabricated a biomimetic soft robot based on the MoO$_2$ actuator, which can locomote spontaneously and climb up the stairs directionally. The inchworm is a kind of soft invertebrate in nature with a distinctive way of crawling. It uses the stretching and contraction of the back muscle to realize the directional crawling motion. The actuator's climbing process can be simply divided into two steps:

(1) When the light is turned on, the actuator will absorb energy and generate heat. The actuator becomes flat with the body stretching to drive the head forward since the tail is stuck.

(2) When the light is turned off, the temperature will be down and the actuator will recovery to bended state, and since the head is hooked on stair, the body is arched to drive the tail to move forward.

Through the alternate motion of stretching and bending, the actuator realizes the directional climbing. The process is shown in **Figure 4.5.1**, **Figure 4.5.2**, and **Movie 4.5.1**. The "inchworm" robot was originally at rest, then the infrared lamp was switched on and the robot started to stretch. Once its head reached the next step, the lamp was switched off for it to bend and its tail finally reached the next step.
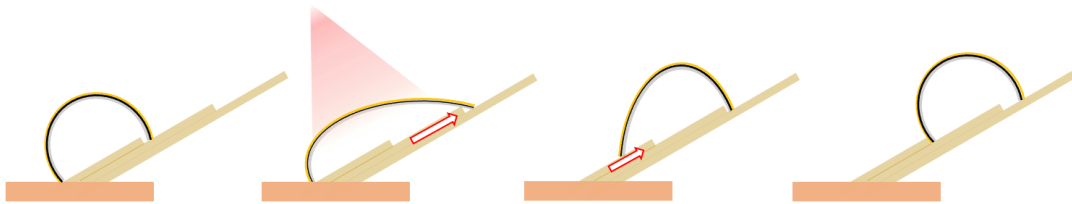
Figure 4.5.1 Schematic illustrations of the "inchworm" robot climbing up the stairs
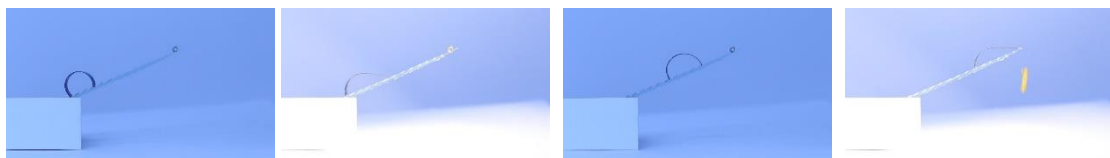
Figure 4.5.2 Optical images of the "inchworm" robot climbing up the stairs and pushed a PI cylinder off

Conclusion

This thesis explored Laser-induced MoO_2-based materials and their applications in bioelectronics and soft robotics.

SEBS was first adopted as substrate mainly because of its breathable, flexible characteristics and chemical stability. We then investigated direct laser scribing, a method enabling excellent control over the manipulation of fabricating MoO_2, an attractive transition metal oxide with low metal resistivity, high melting point and high chemical stability. Combining the characteristics of porous SEBS and DLS-MoO_2, we fabricated a material promising in flexible electronics and soft robotics.

By following electrode modifications and functionalization, we manufactured multifunctional flexible wearable epidermal devices. Assembled by electrophysiological sensors, temperature sensor, UV sensor, humidity sensor, alcohol sensor, NH_3 sensor, and the achieved SEBS-MoO_2 based sensors can monitor information such as electrocardiogram (ECG), electroencephalogram (EEG), temperature, humidity, UV, alcohol and NH_3 concentration. Furthermore, photo actuates soft robotics based on the photothermal transformation of MoO_2 have also been developed. Mechanically assembled 3D structures and a biomimetic self-locomotive "inchworm" robot were manufactured. The SEBS-MoO_2 materials presented in this work open a novel view for the fabrication of flexible epidermal electronics.

Reference

1. Gao, W., et al., *Flexible Electronics toward Wearable Sensing.* Accounts of Chemical Research, 2019. **52**(3): p. 523-533.

2. Kim, J., et al., *Wearable biosensors for healthcare monitoring.* Nat Biotechnol, 2019. **37**(4): p. 389-406.

3. Ray, T.R., et al., *Bio-Integrated Wearable Systems: A Comprehensive Review.* Chemical Reviews, 2019. **119**(8): p. 5461-5533.

4. Someya, T., Z. Bao, and G.G. Malliaras, *The rise of plastic bioelectronics.* Nature, 2016. **540**(7633): p. 379-385.

5. Wang, C.F., et al., *Materials and Structures toward Soft Electronics.* Advanced Materials, 2018. **30**(50).

6. Yang, Y.R. and W. Gao, *Wearable and flexible electronics for continuous molecular monitoring.* Chemical Society Reviews, 2019. **48**(6): p. 1465-1491.

7. Jiang, Z., et al., *Highly Stretchable Metallic Nanowire Networks Reinforced by the Underlying Randomly Distributed Elastic Polymer Nanofibers via Interfacial Adhesion Improvement.* Advanced Materials, 2019. **31**(37).

8. Jin, H., et al., *Highly Durable Nanofiber-Reinforced Elastic Conductors for Skin-Tight Electronic Textiles.* Acs Nano, 2019. **13**(7): p. 7905-7912.

9. Miyamoto, A., et al., *Inflammation-free, gas-permeable, lightweight, stretchable on-skin electronics with nanomeshes.* Nature Nanotechnology, 2017. **12**(9): p. 907-+.

10. Sun, B., et al., *Gas-Permeable, Multifunctional On-Skin Electronics Based on Laser-Induced Porous Graphene and Sugar-Templated Elastomer Sponges.* Advanced Materials, 2018. **30**(50).

11. Bandodkar, A.J., et al., *Tattoo-based potentiometric ion-selective sensors for epidermal pH monitoring.* Analyst, 2013. **138**(1): p. 123-128.

12. Bandodkar, A.J., W. Jia, and J. Wang, *Tattoo-Based Wearable Electrochemical Devices: A Review.* Electroanalysis, 2015. **27**(3): p. 562-572.

13. Bandodkar, A.J., et al., *Epidermal tattoo potentiometric sodium sensors with wireless signal transduction for continuous non-invasive sweat monitoring.* Biosensors & Bioelectronics, 2014. **54**: p. 603-609.

14. Guinovart, T., et al., *A potentiometric tattoo sensor for monitoring ammonium in sweat.* Analyst, 2013. **138**(22): p. 7031-7038.

15. Jia, W., et al., *Electrochemical Tattoo Biosensors for Real-Time Noninvasive Lactate Monitoring in Human Perspiration.* Analytical Chemistry, 2013. **85**(14): p. 6553-6560.

16. Kim, J., et al., *Wearable temporary tattoo sensor for real-time trace metal monitoring in human sweat.* Electrochemistry Communications, 2015. **51**: p. 41-45.

17. Kim, J., et al., *Noninvasive Alcohol Monitoring Using a Wearable Tattoo-Based Iontophoretic-Biosensing System.* Acs Sensors, 2016. **1**(8): p. 1011-1019.

18. Gao, W., et al., *Fully integrated wearable sensor arrays for multiplexed in situ perspiration analysis.* Nature, 2016. **529**(7587): p. 509-+.

19. Wang, L., et al., *Weaving Sensing Fibers into Electrochemical Fabric for Real-Time Health*

Monitoring. Advanced Functional Materials, 2018. **28**(42).

20. Munje, R.D., et al., *A new paradigm in sweat based wearable diagnostics biosensors using Room Temperature Ionic Liquids (RTILs).* Scientific Reports, 2017. **7**.

21. Kinnamon, D., et al., *Portable biosensor for monitoring cortisol in low-volume perspired human sweat.* Scientific Reports, 2017. **7**.

22. Elsherif, M., et al., *Wearable Contact Lens Biosensors for Continuous Glucose Monitoring Using Smartphones.* Acs Nano, 2018. **12**(6): p. 5452-5462.

23. Ma, Z., et al., *Highly Sensitive, Printable Nanostructured Conductive Polymer Wireless Sensor for Food Spoilage Detection.* Nano Letters, 2018. **18**(7): p. 4570-4575.

24. Kim, J.-S., et al., *Tunable Volatile Organic Compounds Sensor by Using Thiolated Ligand Conjugation on MoS2.* Nano Letters, 2014. **14**(10): p. 5941-5947.

25. Smith, A.F., et al., *Bioelectronic protein nanowire sensors for ammonia detection.* Nano Research, 2020. **13**(5): p. 1479-1484.

26. Zhu, C., et al., *Graphene oxide humidity sensor with laser-induced graphene porous electrodes.* Sensors and Actuators B-Chemical, 2020. **325**.

27. Lan, L., et al., *One-step and large-scale fabrication of flexible and wearable humidity sensor based on laser-induced graphene for real-time tracking of plant transpiration at bio-interface.* Biosensors & Bioelectronics, 2020. **165**.

28. Ye, R., D.K. James, and J.M. Tour, *Laser-Induced Graphene.* Accounts of Chemical Research, 2018. **51**(7): p. 1609-1620.

29. Xu, Y., et al., *Self-Assembled Graphene Hydrogel via a One-Step Hydrothermal Process.* Acs Nano, 2010. **4**(7): p. 4324-4330.

30. Ye, R., et al., *High Performance Electrocatalytic Reaction of Hydrogen and Oxygen on Ruthenium Nanoclusters.* Acs Applied Materials & Interfaces, 2017. **9**(4): p. 3785-3791.

31. Chen, Z., et al., *Three-dimensional flexible and conductive interconnected graphene networks grown by chemical vapour deposition.* Nature Materials, 2011. **10**(6): p. 424-428.

32. Choi, B.G., et al., *3D Macroporous Graphene Frameworks for Supercapacitors with High Energy and Power Densities.* Acs Nano, 2012. **6**(5): p. 4020-4028.

33. Lin, J., et al., *Laser-induced porous graphene films from commercial polymers.* Nature Communications, 2014. **5**.

34. Dong, Y., S.C. Rismiller, and J. Lin, *Molecular dynamic simulation of layered graphene clusters formation from polyimides under extreme conditions.* Carbon, 2016. **104**: p. 47-55.

35. Ye, R., et al., *Laser-Induced Graphene Formation on Wood.* Advanced Materials, 2017. **29**(37).

36. Peng, Z.W., et al., *Flexible Boron-Doped Laser-Induced Graphene Microsupercapacitors.* Acs Nano, 2015. **9**(6): p. 5868-5875.

37. Nam, K.-H., et al., *Laser Direct Write of Heteroatom-Doped Graphene on Molecularly Controlled Polyimides for Electrochemical Biosensors with Nanomolar Sensitivity.* Carbon, 2021.

38. Chyan, Y., et al., *Laser-Induced Graphene by Multiple Lasing: Toward Electronics on Cloth, Paper, and Food.* Acs Nano, 2018. **12**(3): p. 2176-2183.

39. Singh, S.P., et al., *Sulfur-Doped Laser-Induced Porous Graphene Derived from*

Polysulfone-Class Polymers and Membranes. Acs Nano, 2018. **12**(1): p. 289-297.

40. *Oxide Nanostructures: Growth, Microstructures, and Properties.* Oxide Nanostructures: Growth, Microstructures, and Properties, ed. A.K. Srivastava. 2013. 1-389.

41. Ogale, S.B., T.V. Venkatesan, and M.G. Blamire, *Functional Metal Oxides New Science and Novel Applications Preface.* Functional Metal Oxides: New Science and Novel Applications, ed. S.B. Ogale, T.V. Venkatesan, and M.G. Blamire. 2013. XV-XVI.

42. Hong, S., et al., *Digital selective laser methods for nanomaterials: From synthesis to processing.* Nano Today, 2016. **11**(5): p. 547-564.

43. Hwang, D., et al., *Nanoscale laser processing and diagnostics.* Applied Physics a-Materials Science & Processing, 2009. **96**(2): p. 289-306.

44. Mincuzzi, G., et al., *Laser Processing in the Manufacture of Dye-Sensitized and Perovskite Solar Cell Technologies.* Chemelectrochem, 2016. **3**(1): p. 9-30.

45. Bharadwaja, S.S.N., et al., *Excimer laser assisted re-oxidation of BaTiO3 thin films on Ni metal foils.* Journal of Applied Physics, 2016. **119**(2).

46. Kang, M.-G., et al., *Large in-plane permittivity of Ba0.6Sr0.4TiO3 thin films crystallized using excimer laser annealing at 300 degrees C.* Applied Physics Letters, 2012. **101**(24).

47. Peng, Y., et al., *Nanoporous polyethylene microfibres for large-scale radiative cooling fabric.* Nature Sustainability, 2018. **1**(2): p. 105-112.

48. Robinson, A.J., *Clinical electrophysiology: electrotherapy and electrophysiologic testing.* 2008: Lippincott Williams & Wilkins.

49. Webster, J.G., *Medical instrumentation-application and design.* Journal of Clinical Engineering, 1978. **3**(3): p. 306.

50. Somers, V.K., et al., *Sympathetic neural mechanisms in obstructive sleep apnea.* J Clin Invest, 1995. **96**(4): p. 1897-904.

51. Modarreszadeh, M., et al. *Wireless, 32-channel, EEG and epilepsy monitoring system.* in *International Conference of the IEEE Engineering-in-Medicine-and-Biology-Society.* 1997. Chicago, Il.

52. Serup, J., G.B. Jemec, and G.L. Grove, *Handbook of non-invasive methods and the skin.* 2006: CRC press.

53. Heikenfeld, J., et al., *Wearable sensors: modalities, challenges, and prospects.* Lab Chip, 2018. **18**(2): p. 217-248.

54. Liu, R.P., et al., *Flexible Temperature Sensors.* Frontiers in Chemistry, 2021. **9**.

55. Asib, N.A.M., et al., *Developing high-sensitivity UV sensors based on ZnO nanorods grown on TiO2 seed layer films using solution immersion method.* Sensors and Actuators A: Physical, 2020. **302**: p. 111827.

56. Ozel, K. and A. Yildiz, *SnO2/ZnO/p-Si and SnO2/TiO2/p-Si heterojunction UV photodiodes prepared using a hydrothermal method.* Sensors and Actuators A: Physical, 2020. **315**: p. 112351.

57. Zou, W., et al., *Skin color-specific and spectrally-selective naked-eye dosimetry of UVA, B and C radiations.* Nature Communications, 2018. **9**(1): p. 3743.

58. Qin, L.G., et al., *Economic Friendly ZnO-Based UV Sensors Using Hydrothermal Growth: A Review.* Materials, 2021. **14**(15).

59. Blank, T., L. Eksperiandova, and K. Belikov, *Recent trends of ceramic humidity sensors development: A review.* Sensors and Actuators B: Chemical, 2016. **228**: p. 416-442.

60. Chen, Z. and C. Lu, *Humidity sensors: a review of materials and mechanisms.* Sensor letters, 2005. **3**(4): p. 274-295.

61. Peng, Y., et al., *Research advances in microfiber humidity sensors.* Small, 2018. **14**(29): p. 1800524.

62. Seiyama, T., N. Yamazoe, and H. Arai, *Ceramic humidity sensors.* Sensors and Actuators, 1983. **4**: p. 85-96.

63. Gao, W., et al., *Direct laser writing of micro-supercapacitors on hydrated graphite oxide films.* Nature nanotechnology, 2011. **6**(8): p. 496-500.

64. NaderiNasrabadi, M., Y. Mortazavi, and A.A. Khodadadi, *Highly sensitive and selective Gd2O3-doped SnO2 ethanol sensors synthesized by a high temperature and pressure solvothermal method in a microreactor.* Sensors and Actuators B: Chemical, 2016. **230**: p. 130-139.

65. Wongrat, E., et al., *Low temperature ethanol response enhancement of ZnO nanostructures sensor decorated with gold nanoparticles exposed to UV illumination.* Sensors and Actuators A: Physical, 2016. **251**: p. 188-197.

66. Thungon, P.D., et al., *Advances in developing rapid, reliable and portable detection systems for alcohol.* Biosensors and Bioelectronics, 2017. **97**: p. 83-99.

67. Mirzaei, A., et al., *Highly stable and selective ethanol sensor based on α-Fe2O3 nanoparticles prepared by Pechini sol–gel method.* Ceramics International, 2016. **42**(5): p. 6136-6144.

68. Abbasi, A. and J.J. Sardroodi, *Investigation of the adsorption of ozone molecules on TiO2/WSe2 nanocomposites by DFT computations: Applications to gas sensor devices.* Applied Surface Science, 2018. **436**: p. 27-41.

69. Chen, W.Y., et al., *Nanohybrids of a MXene and transition metal dichalcogenide for selective detection of volatile organic compounds.* Nature communications, 2020. **11**(1): p. 1-10.

70. Hong, Y., et al., *Gas-sensing characteristics of exfoliated WSe2 field-effect transistors.* Journal of Nanoscience and Nanotechnology, 2017. **17**(5): p. 3151-3154.

71. Medina, H., et al., *Wafer-Scale Growth of WSe2 Monolayers Toward Phase-Engineered Hybrid WO x/WSe2 Films with Sub-ppb NO x Gas Sensing by a Low-Temperature Plasma-Assisted Selenization Process.* Chemistry of Materials, 2017. **29**(4): p. 1587-1598.

72. Yoo, K.-P., et al., *Effects of O2 plasma treatment on NH3 sensing characteristics of multiwall carbon nanotube/polyaniline composite films.* Sensors and Actuators B: Chemical, 2009. **143**(1): p. 333-340.

73. Xu, K., et al., *A peculiar cyclic voltammetric behavior of polyaniline in acetonitrile and its application in ammonia vapor sensor.* Journal of Electroanalytical Chemistry, 2007. **608**(2): p. 141-147.

74. Pushkarsky, M., M. Webber, and C. Patel, *Ultra-sensitive ambient ammonia detection using CO 2-laser-based photoacoustic spectroscopy.* Applied Physics B, 2003. **77**(4): p. 381-385.

75. Ma, Z., et al., *Highly Sensitive, Printable Nanostructured Conductive Polymer Wireless Sensor for Food Spoilage Detection.* Nano Lett, 2018. **18**(7): p. 4570-4575.